62

An Experimental Study of Nanobubbles on Hydrophobic Surfaces

by

Abhinandan Agrawal

B. Tech., Mechanical Engineering (2003)
Indian Institute of Technology, Kanpur, India

Submitted to the Department of Mechanical Engineering
in partial fulfillment of the requirements for the degree of

Master of Science in Mechanical Engineering

at the

MASSACHUSETTS INSTITUTE OF TECHNOLOGY
[September 2005]
August 2005

Author _____
Department of Mechanical Engineering
August 20, 2005

Certified by _____
Gareth H. McKinley
Professor of Mechanical Engineering
Thesis Supervisor

Accepted by _____
Lallit Anand
Professor of Mechanical Engineering
Chairman, Department Committee on Graduate Students

An Experimental Study of Nanobubbles on Hydrophobic Surfaces

by
Abhinandan Agrawal

Submitted to the Department of Mechanical Engineering
on August 20, 2005, in partial fulfillment of the
requirements for the degree of
Master of Science in Mechanical Engineering

Abstract

With the recent development of microfluidic systems, miniaturization of flow devices has become a real challenge. Microchannels, however, are characterized by a large surface area-to-volume ratio so that surface properties strongly affect flow resistance in sub-micrometer devices. Recent studies in the literature have opened up the possibility of a controlled realization of *nanobubbles*—found to exist primarily on hydrophobic surfaces—that can play an important role in changing the hydrodynamic boundary condition at the fluid-solid interface giving rise to considerable reduction in friction of the fluid flow past the solid boundaries. In this study, we seek to increase our understanding of the formation, morphology and stability of nanobubbles. Further, we seek to exploit the dependence of nanobubble formation on surface hydrophobicity to provide a means for controlling hydrodynamic boundary conditions at the solid-liquid interface.

The formation of nanobubbles at solid-liquid interfaces has been studied using the atomic force microscopy (AFM) imaging technique. Nanobubble formation strongly depends on both the hydrophobicity of the solid surface and the polarity of the liquid subphase. First, a number of homogenous surfaces are used as solid substrates to understand and analyze the formation and distribution of nanobubbles on homogenous surfaces with differing degrees of hydrophobicity. While nanobubbles do not form on flat hydrophilic surfaces immersed in water, they appear spontaneously at the interface of water against smooth, hydrophobic surfaces. From the experimental evidence, we draw the conclusion that the features observed in the AFM images are deformable, air-filled bubbles. In addition to the hydrophobicity of the solid surface, differences in solubility of air between two miscible fluids can also lead to nucleation and growth of nanobubbles. We observe that nanobubbles appear at the interface of water against hydrophilic silicon oxide surfaces after in-situ mixing of ethanol and water in the fluid-cell.

While for most part, the shapes of the nanobubbles are well approximated by spherical caps with width much larger than the height; in the vicinity of the three phase contact line, the shapes deviate significantly from the spherical cap profile to merge with the solid surface at a slope of < 0.05. This deviation in the interfacial profile from the spherical cap shape is due to long-range van der Waals forces, which are relevant at a spatial scale of few nanometers from the solid surface. We quantify the morphological distribution of nanobubbles by evaluating several important bubble parameters including surface coverage and radii of curvature. In conjunction, with an analytical model available in the literature, we use this information to estimate that the present nanobubble morphology may give rise to

slip lengths $\sim$1-2 μm in pressure driven flows for water flowing over a typical hydrophobic surface. The consistency of the calculated slip length with experimental values reported recently in the literature, suggests that the apparent fluid slip observed experimentally at hydrophobic surfaces may indeed arise from the presence of nanobubbles. Further, trends are established between different morphological parameters and surface hydrophobicity. Bubbles are found to get bigger, wider and less-frequent in number with increasing surface hydrophobicity. The pressure inside the bubble is found to decrease with an increase in the surface hydrophobicity.

The presence of nanobubbles is controlled using nanopatterned surfaces possessing repeating patterns of polystyrene (hydrophobic domains) and polymethyl-methacrylate (hydrophilic domains). For nanobubbles to be present, we find that, in addition to controlling the degree of surface hydrophobicity, it is important for the spatial dimensions of the hydrophobic domains on the nanopatterned surface to be commensurate with the equilibrium topology of the nanobubbles. To the best of our knowledge, this is the first experimental study in which chemically inhomogeneous surfaces are used to probe the existence of nanobubbles.

Thermodynamic issues related to formation and stability of nanobubbles are also discussed. The effects of line tension at the three-phase contact line is discussed for the observed set of nanobubbles. Further, the length-scale of a typical nanobubble is found to be comparable to the mean-free-path of gas molecules inside the bubble. The above fact suggests that the Young-Laplace equation —used in continuum theories for calculating pressure difference across an interface—may not be applicable in its unmodified form for the case of nanobubbles. It is noteworthy that the anomalously high pressure values obtained using this equation for nanobubbles have been the reason for much debate on the stability of nanobubbles.

Thesis Supervisor: Gareth H. McKinley
Title: Professor of Mechanical Engineering

Acknowledgements

First, I would like to express my deepest gratitude to my advisor Professor Gareth H. McKinley for his expert advice and patient guidance all throughout this research project. Without his constant encouragement this work would not have been possible. It was a privilege for me to work with him.

A special thanks goes to my group mates (Randy, Giorgia, Trevor, Suraj, Roger, Shawna, Stephen, Monica, Lucy, Volkmar, Young Jun, Chris, Nitin, Shankar, Ryan and Tim) at the Non-Newtonian Fluids lab for the endless discussions and support throughout the last two years.

Special thanks to Nitin for many stimulating discussions on my research and to Roger for finding me the right patch to all the software!

I would also like to thank National Science Foundation (NSF) for monetary support.

Finally, I would like to thank my parents for their endless love, without which I wouldn't have come this far.

Contents

List of Figures

List of Tables

Chapter 1

Introduction

1.1 Hydrophilic and hydrophobic surfaces

DIFFERENT surfaces can be broadly categorized into two categories—hydrophilic and hydrophobic—with respect to their behavior towards water. While hydrophilic surfaces have high surface energy and high affinity for water, hydrophobic surfaces are low energy surfaces, and they repel water. Figure 1.1 shows the differences in behavior of hydrophilic and hydrophobic surfaces at different length scales.

At the macroscale, we see a significant difference in the contact angles of water on both the surfaces. While on the hydrophilic surface water spreads out uniformly to give a low value of contact angle, on the hydrophobic surface water does not spread, giving rise to a relatively higher value of contact angle.

At the microscale, we see that the water-side contact angle at the air-water interface is lower in the case of microchannel with hydrophilic walls than in the case of microchannel with hydrophobic walls (Figure 1.1).

At the nanoscale—and this was not known until few years back—topology at the interface of water and flat hydrophilic and hydrophobic surfaces look very different from each other. While flat hydrophilic surfaces appear featureless under water, flat hydrophobic surfaces show close-packed, uniformly-spread, randomly-distributed air-pockets. In literature, these features have been referred to as *nanobubbles*. These bubbles can be observed by carrying out tapping-mode atomic force microscope (AFM) imaging of hydrophobic surfaces in water.

1.2 Hydrophobicity and wetting at small length scales

With the important development of microfluidic systems, miniaturization of flow devices has become a real challenge. A factor, common to all the small length-scale problems in microfluidics is a large value of surface-area-to-volume ratio. Equation 1.1 suggests that

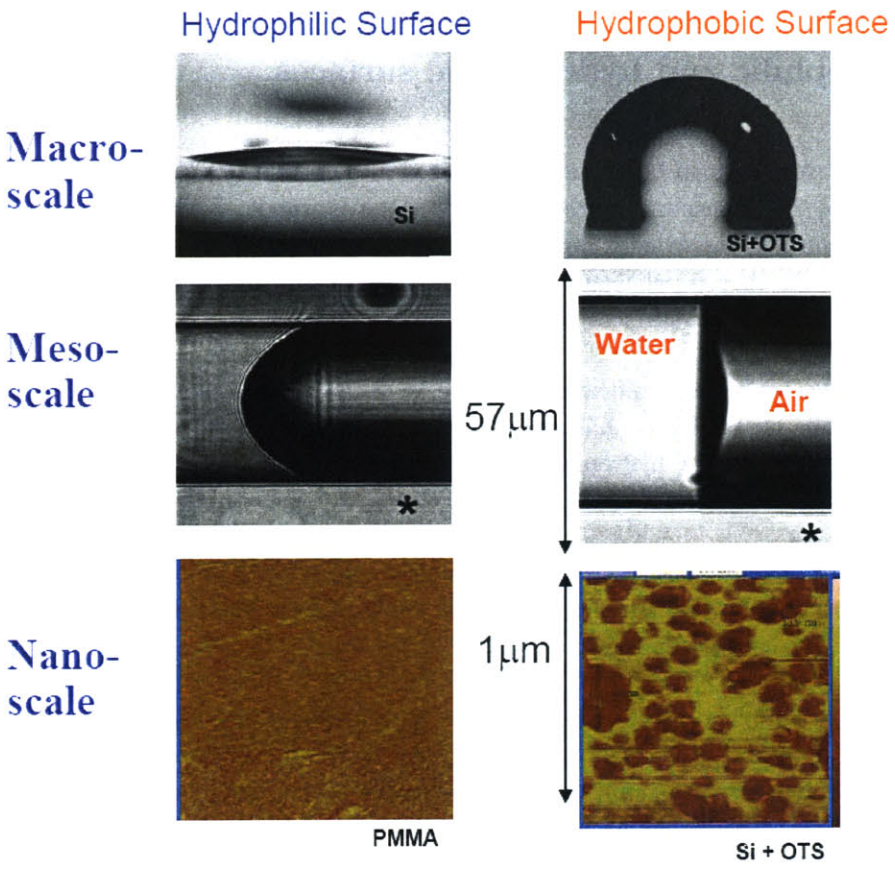

Figure 1.1: An overview of the differences between hydrophilic and hydrophobic surface behavior at different length scales.

as the characteristic length-scale (l) goes down, the ratio of surface area to volume will get larger. The above statement suggests that surface properties will then have a greater impact on liquid-surface interaction at small length scales as compared to bulk properties.

$$\frac{\text{Surface area}\,(l^2)}{\text{Volume}\,(l^3)} \quad \rightarrow \quad \mathrm{O}\left(\frac{1}{l}\right) \tag{1.1}$$

The strength of the interaction between a solid and a liquid is most obviously characterized through the wetting behavior. There are number of studies in literature which show the effect of surface hydrophobicities on wetting phenomena at small length scales. Recently, a large, shear-rate-dependent fluid slip has been measured at partially wetted fluid-solid surfaces [65]. Surfaces with controlled wetting properties have also been used for understanding and fabrication of "self-cleaning" surfaces [13]. Bizzone *et* al. [18] have shown that the concerted effect of wetting properties and the surface roughness may considerably reduce friction and increase fluid-slippage of the fluid past the solid boundaries.

Further, in recent studies [33, 11, 44], hydrophobic surfaces coupled with modern self-assembly and microfabrication techniques have been used to demonstrate the so-called superhydrophobic surfaces, which exhibit a number of new and exciting properties such as extremely high contact angles and very low flow resistance.

In conclusion, the hydrophobicity of solid surfaces influences the solid-liquid interaction at small length scales in an important way. Therefore, the future of further scaling down of microscale devices to even smaller length scales would rest upon—besides other factors—the understanding of the effects of surface properties on the solid-liquid interface.

1.3 Nanobubbles present at the solid-liquid interface

Nanobubbles, with 5–100 nm heights and 0.1–0.8 μm diameters, are found to appear spontaneously at the interface between a polar solvent (e.g. water) saturated with air and hydrophobic surfaces [47, 51, 53, 27, 24, 61, 58]. The presence of these bubbles has been detected by atomic force microscopy [47, 27, 24, 61, 58] as well as other techniques including rapid cyrofixation/freeze fracture and neutron reflectometry [51, 53]. Although the origin of these bubbles is unclear and some debate remains in the literature about their existence [5, 7] they have recently been invoked as a possible origin of number of phenomena, including, the long-range attraction between hydrophobic surfaces immersed in water, the stability of an emulsion without a surfactant, microboiling behavior, mineral flotation, and the rupture of wetting films. Nanobubbles on surfaces can also have significant conse-

quences on the motion of particles in liquids or on the flow of liquids adjacent to surfaces or in capillaries. We can expect a reduction in drag by such nanobubbles, since interfacial slip obviously occurs at a fluid-fluid interface, whereas no-slip boundary conditions are traditionally expected in hydrodynamic flows bounded by solid surfaces. It has also been argued that nanobubbles lead to the frequency-dependent and shear-rate dependent fluid-slip that has been recently observed at partially wetting fluid-solid surfaces [34, 65, 18], and which gives rise to considerable reduction in friction of fluid flow past the solids. From the earlier publications it can be concluded that formation of nanobubbles strongly depends on the properties of the substrates. While they exist primarily on hydrophobic surfaces, they do not appear spontaneously on hydrophilic surfaces, unless they form from the differences in the solubility of air between two miscible fluids [35].

1.4 Motivation for studying nanobubbles

There are numerous reasons which have motivated us to pursue this study on nanobubbles. Some of the reasons are given below:

- Nanobubbles offer a novel approach for reducing the drag on the macroscopic objects moving in water, as it provides a free-slip boundary condition at the solid-liquid interface.
- Nanobubbles are selective in their occurrence. While they appear on certain surfaces (mostly hydrophobic), they do not form spontaneously on others (mostly hydrophilic). This phenomena can be exploited to gain a control over the presence and spatial-extent of nanobubbles with the help of surfaces patterned with hydrophobic and hydrophilic domains. By controlling the presence of nanobubbles at the solid-liquid interface, we can indirectly control the macroscale wetting behavior.
- While the experimental evidence, as reviewed elsewhere [8], shows that nanobubbles exist and are the origin of the measured long-ranged hydrophobic attractions, the theoretical understanding of the nanobubble phenomenon is not so advanced. There remain unanswered a number of questions regarding their shapes, origin and stability. There is also an apparent paradox between the Young-Laplace equation and the observed occurrence and stability of nanobubbles. Thus, study of nanobubbles would help us increase our understanding of a nanoscale phenomena where unmodified macroscale thermodynamic relations might not be applicable.

(a) Miniaturizing and integrating all the laboratory processes on to a microchip device (actual length of the chip is ~1 inch)

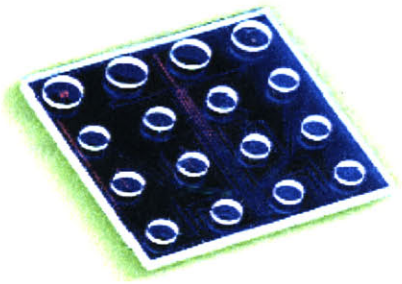

(b) Microfluidic microchip based on "lab on a chip" technology fabricated in glass

Figure 1.2: Lab on a chip technology [16]

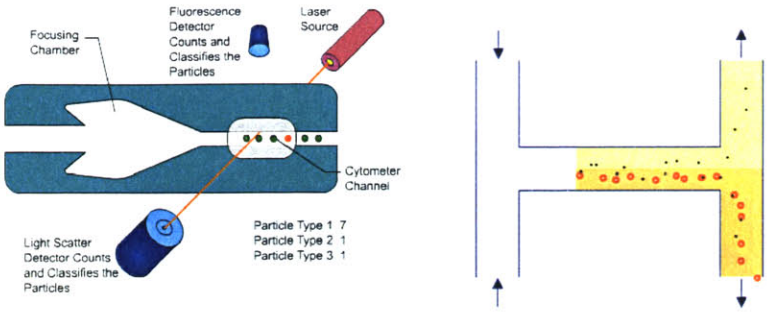

(a) Microcytometer (b) H-filter

Figure 1.3: Fluid based microelectromechanical-systems (MEMS) devices [25]

1.5 Applications

The most obvious example of a system where understanding of liquid-surface interaction at small length scales can be of much importance has been often referred to as the "lab on a chip" technology[16] (Figure 1.2), in which integrated microfabricated devices can be used for chemical analysis and for controlling chemical reactions of sub-nanoliter volumes. It is easy to notice that one of the main requirements for this system to be efficient is low friction coefficient or in other words, high flow rates without the application of high pumping force. Equation 1.2 suggests that changing the bulk properties will not have drastic consequences on frictional properties at solid-liquid interface, but changing the surface properties will. For a given fluid flow-rate, the pressure head required to drive the flow varies as inverse of R^4. Thus for small systems, a higher pressure would be required to maintain the same flow-rate.

$$Q = \frac{\pi}{8}\frac{(\Delta P)R^4}{\mu L} \tag{1.2}$$

Another example consists of fluid based MEMS devices. Figure 1.3 shows two of several MEMS devices that have already started getting commercialized. Figure 1.3(a) shows a microcytometer, where the idea is to miniaturize flow cytometry–the measurement of cell properties as they move, or flow, in liquid suspension. Figure 1.3(b) shows a H-filter, where diffusion can be used to filter unwanted components or to extract desired components from one of several fluids being simultaneously processed.

Another example where liquid-surface interaction exists at small length-scale and has important consequences for the process is nanoimprint lithography. Figure 1.4 shows the stamp imprinting and stamp releasing steps during the imprinting process. It is important to gain control over the frictional and adhesional properties at the polymer-stamp interface to make sure that there is no spillage of the polymer over undesired locations on the substrate and that the polymer does not get carried away along with the stamp.

Further, key advances in the understanding and fabrication of surfaces with controlled wetting properties can also make the dream of contamination-free surfaces come true [13]. Figure 1.5 shows an example from nature where structural features on the plant leaves, together with the waxy surface chemistry, render the leaves non-wettable. Using this principle for practical applications, efforts are being made to develop various self-cleaning solid surfaces.

1.6 Literature survey on nanobubbles

For the past two decades there has been energized debate over the origin of the attractive force observed between macroscopic hydrophobic surfaces in water. The "hydrophobic force" [29] is responsible for many theories as well [5, 57, 58]. The bridging of submicroscopic nanobubbles that were seen on the surface of a hydrophobic material [5, 6] in water is one likely explanation [5, 42] for the widely studied long-range attraction measured with the surface force apparatus (SFA) between hydrophobic surfaces [43, 29]. Several groups directly visualized nanobubbles associated with the solute/solvent interface using atomic force microscopy (AFM) and force spectroscopy. Attard and co-workers imaged a layer of bubbles as a non-regular pattern on silanized glass using tapping-mode AFM [7, 57, 58]. The bubbles were distinctly non-circular and exhibited typical diameters of $\sim$ 80 nm and height around 30 nm. In contrast, Ishida *et* al. [27] measured nanobubbles formed on silanized Si (100) wafers that had quite similar dimensions but showed a circular footprint. Although the bubbles measured by Ishida had a circular base, the line scans showed that the shape of the bubble surface was non-spherical. Simonsen *et* al. [47] observed a nearly close-packed and uniform population of bubbles with a circular footprint on polystyrene with area coverage of nanobubbles around 61%. In another study by the same group [51], neutron reflectivity measurements were done for the hPS/D_2O interface and an interfacial region of reduced scattering length density of width 1–5 nm was found to exist. Spherical nanobubbles were also reported to be formed on mica and graphite surfaces by in-situ mixing of ethanol and water [36, 37].

However, in these cases the formation of bubbles is probably not driven by a mismatch

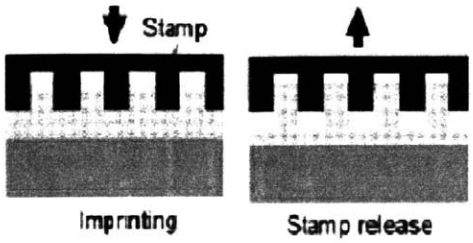

Figure 1.4: Schematic of the stamp imprinting and releasing steps in nanoprinting [10]

in hydrophobicity between the bulk liquid sub-phase and the solid surface [47]. Yang *et* al. [61] observed formation of very small gas bubbles on hydrophobic surfaces with different degrees of hydrophobicity and nanometer-scale surface roughness. The general understanding in the literature was that the bubbles could only be seen with AFM operated in tapping mode and not in contact mode until Holmberg *et* al. [24] imaged nanobubbles on ultra-flat gold surfaces using contact mode AFM. All the above experimental studies are mostly carried out with AFM. Switkes *et* al. [53] used an innovative technique *rapid cyrofixation freeze fracture* for study of nanobubbles at solid-liquid interfaces to image nanobubbles on a silanized silicon surface. Although there is some literature available on nanobubbles, there are only few papers which have in-depth quantitative analysis of different morphological parameters for nanobubbles—namely height, diameter, radius of curvature, pressure, volume, area coverage—along with their variation with surface hydrophobicity. Besides experimentally observing the nanobubbles, a computational model for calculating slippage at the hydrophobic walls due to nanobubbles [34, 18] is also discussed in the literature.

Appendix B gives the summary of relevant results from above studies in a tabular format.

1.7 Objectives

The objectives of the present study are as follows:

- To understand and analyze the formation and distribution of nanobubbles on homogenous surfaces with different hydrophobicities
- To carry out an extensive quantitative-statistical analysis on nanobubbles to determine various bubble parameters

Figure 1.5: An almost spherical-shaped water droplet on a non-wettable plant leaf [23]

- To establish the trends between different morphological parameters for nanobubbles and surface hydrophobicity.
- To demonstrate a possibility of controlling the location and spatial-extent of nanobubbles with the help of nanopatterned surfaces.
- To address the thermodynamic issues related to the formation and stability of nanobubbles

1.8 Chapter descriptions

Chapter 2 describes the general methodology adopted in this study. This chapter includes description of different kinds of surfaces used in the study, their method of preparation, instrumentation, tip characterization, calibration results, and a few useful post-processing tools. AFM tip-sample interaction force calibration plots are also presented here. The force calibration plots are important for quantifying energy transfer from the scanning probe to bubble. Chapter 3 contains results (along with detailed qualitative analysis) from experiments with different homogenous hydrophobic and hydrophilic surfaces. The effect of different environmental conditions on nanobubbles along with plenty of experimental evidences in favor of nanobubbles are also presented here.

Chapter 4 contains results from experiments with different nanopatterned surfaces. In chapter 5, quantitative and statistical analysis of the images obtained in chapter 3 are presented.

Various bubble parameters are derived for different surface hydrophobicities to establish the trends in these parameters with surface hydrophobicity. This chapter also includes a discussion on line tension, which is found to be relevant at the length-scale of the given problem.

Chapter 6 includes a discussion on the physical understanding behind the formation and stability of the nanobubbles. A discussion on the validity of macroscale thermodynamic relations at small length-scales is also presented in this chapter. Chapter 7 contains conclusions and future work.

Chapter 2

Methodology

IN this chapter, the general methodology adopted in this study is discussed, which includes description of different kinds of surfaces along with their method of preparation, instrumentation, tip-characterization, calibration results, and a few post-processing tools.

2.1 Sample preparation

A number of different surfaces—both homogenous and chemically patterned—were used in this study to probe the existence of nanobubbles. Description of these surfaces along with their method of preparation is discussed in this section.

2.1.1 Homogenous surfaces

A number of homogenous surfaces with wide range of surface hydrophobicities are used in this study. Figure 2.1 lists all the homogenous surfaces used, along with their contact angle values with water. The surfaces are arranged in increasing order of their hydrophobicities or equivalently, increasing order of their contact angle values. For experiments in this study to be meaningful, it is important that the homogenous surfaces be very smooth. Since one of the aims of this research work is to study the sole effect of surface hydrophobicity on morphology of nanobubbles, it is important to get rid of the other factors including roughness (generated by the presence of surface contaminants), which might affect the nanobubble formation.

2.1.1.1 Silanized and non-silanized glass/silicon surfaces

Silanization is one of the simpler ways to produce hydrophobic surfaces. Silicon and glass wafers are used in this study along with different silanes to give surfaces with a wide range of contact angles.

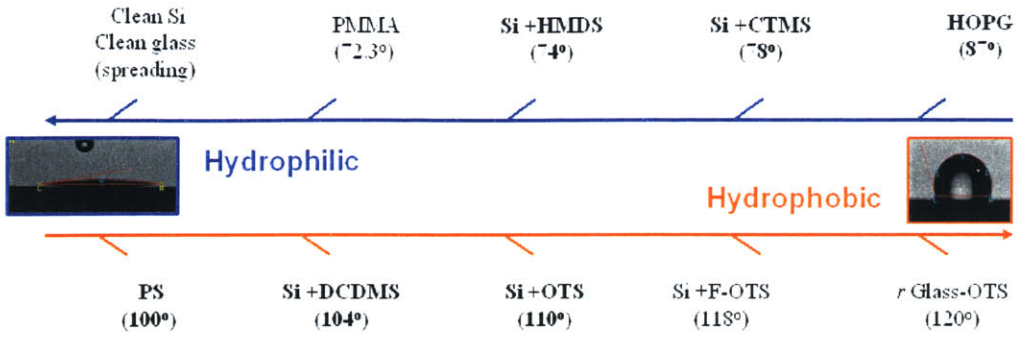

Figure 2.1: List of homogenous surfaces (along with their contact angle values with water) used in this study (samples with names in bold have been studied for nanobubbles by other groups)

Glass wafers were first cut from glass slides which were obtained from *VWR Scientific, Inc.* A rigorous cleaning procedure was adopted to get rid of any contaminants stuck to the wafers. The step by step process is as follows:

1. Using a water bath, a solution containing 5 parts water and 1 part ammonium hydroxide (NH_3OH) was heated to $\sim 80°C$. The glass wafers were immersed during this step.
2. One part hydrogen peroxide (H_2O_2) was added to the solution, and the solution was then maintained at $80 - 85°C$ for ~ 20 minutes.
3. The cleaning solution was poured out of the beaker. The same beaker was then used as a rinsing bath. Wafers were then rinsed 3 times with deionized water.
4. Samples which were still in the original beaker were dried using dry nitrogen gas. The other way to dry the samples was to put them in an oven at $100°C$ for as long as necessary. In this case, beaker was covered to avoid contamination by dust particles in the oven.

Following the above procedure, the glass slides were found to be very smooth as observed with AFM (images in chapter 3). The glass wafers cleaned using the above procedure were found to be extremely hydrophilic with water spreading over them instantly.

To hydrophobize the wafers, they were dipped in a 0.01 M solution of silane in toluene. The wafers were kept for about 30 minutes after which they are rinsed thoroughly with toluene, followed by chloroform. The last step of rinsing is important and has to be carefully done to remove any amount of silane left unused over the surface. Silanes tend to polymerize quickly

in presence of either water or water vapor and thus unused silanes left over the surface can lead to formation of contaminants when the sample comes in contact with ambient water vapor. It is also found that rinsing with ethanol (95 % pure) after chloroform results in a "foggy" surface. This may be due to silane coming in contact with water molecules present in 95 % by vol. ethanol solution. This observation was also made by Mao *et* al. [40].

Silicon wafers were obtained from *MEMC Electronic Materials.* To prepare both hydrophobic and hydrophilic silicon surfaces, a similar procedure to one used for glass wafers was used. However this time, instead of a solution of ammonium hydroxide and hydrogen peroxide, a solution of NOCHROMIX® and conc. sulfuric acid (a variant of "pirhana solution") was used. NOCHROMIX® is a patented, white crystalline, inorganic oxidizer, which when mixed with sulfuric acid, forms a clear, strong cleaning solution, which can chemically clean a surface without leaving residue on the surface (neither detergent film nor heavy metal residue). The hydrophobization procedure was similar to that used for glass surfaces.

Different silanes are used in this study to give different surface hydrophobicities. Both silicon and glass surfaces upon treatment with a particular silane led to the same contact angle value with water. This observation suggests that chemistry of the exposed surface is governed by the chemistry of silane monolayer rather than chemistry of underlying substrate itself. Octadecyltricholorsilane (OTS), hexadimethylsilazane (HMDS), dichlorodimethylsilane (DCDMS), perflurotrichloroctylsilane (pFTCS), chlorotrimethylsilane (CTMS) are the names of different silanes used in this study. Respective contact angles of water on these surfaces are listed in Figure 2.1.

2.1.1.2 Polymeric surfaces

Plain polystyrene (PS) and polymethylmethacrylate (PMMA) surfaces were also used in this study. These surfaces were provided to us by Prof. Russell's group at UMass. Amherst. Spin-coating technique was used to prepare these surfaces. For PS and PMMA substrates, 1 wt % of polymer in toluene was found to give ~30 nm thick polymer layer in a typical spin-coating process (at ~ 3000 rpm). Higher molecular weight samples were found to work better because of dewetting problems on silicon wafer. Finally, 3 % weight solutions of PS (Mn: ~250k) and PMMA (Mn: ~150k) were used to give ~90 nm thick film of these polymers on silicon wafers. The roughness measurements on these surfaces are discussed in chapter 3.

2.1.2 Highly oriented pyrolytic graphite (HOPG) surfaces

Highly oriented pyrolytic graphite (HOPG) surfaces obtained from *SPI Supplies*® were also used as one of the substrates. There were many reasons behind selection of this surface as one of the substrates. First, HOPG surfaces are extremely smooth, which satisfies one of the important requirements of experiments on homogenous surfaces in this work. There are plenty of data and results available on HOPG from different studies in literature. The fact that water on graphite can also be related to water on and inside the carbon nanotubes (CNT) makes the study of these surfaces more relevant. Last but not the least, the contact angle of water on HOPG surface is found to be around 90°, which puts the surface in between the regimes of hydrophilic and hydrophobic substrates.

HOPG, because of its layered structure, cleaves almost like mica. The usual approach taken to prepare sample of HOPG is to take a piece of tape (e.g. *3M*® "Scotch Brand" double sided tape), press it onto the flat surface and then pull it off. The tape invariably takes with itself a thin layer of HOPG. This freshly cleaved surface is what is used as sample substrate material.

2.1.3 Nanopatterned surfaces

Nanopatterned surfaces used in this study were procured from two research groups. One of the groups is Prof. T. P. Russell's research group at UMass. Amherst, where diblock-copolymers were used to fabricate nanopatterned surfaces. The other group is Prof. P. T. Hammond's research group at MIT, where polymer spin-transfer printing was used to make nanopatterned surfaces. Procedures for preparation of these surfaces are discussed in brief here, and in detail elsewhere [3].

Surfaces prepared using diblock-copolymer technique

The method of preparation of nanopatterned surfaces using block-copolymer technique used here, is mentioned in detail in literature ([45, 46, 62]), and it is shown in the schematic diagram in Figure 2.2.

The step by step procedure is as follows:

1. HO-functionalized random copolymer solution (1 wt% in toluene) is spin-coated on a silicon wafer, giving 1 micron thick layer of polymer solution. After annealing in the vacuum oven at 170°C for 3 days, residual unreacted polymers are rinsed using toluene

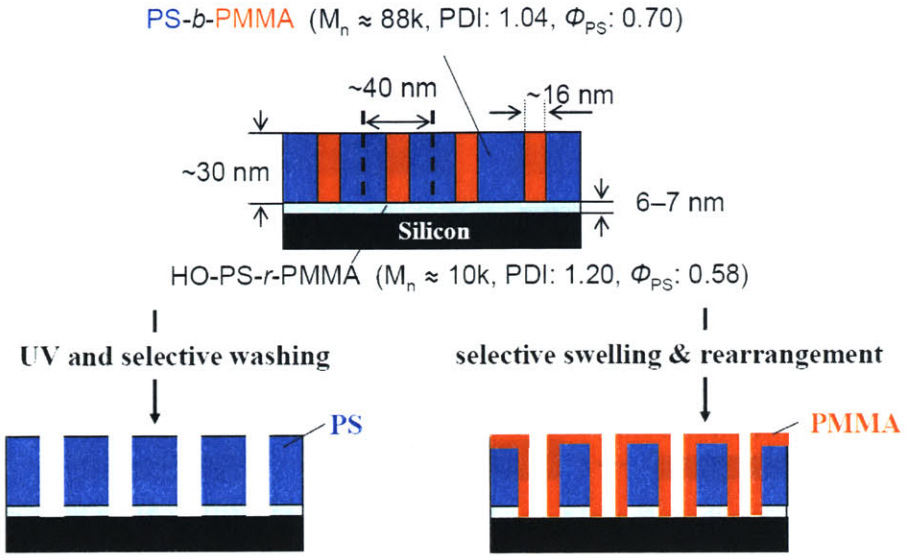

Figure 2.2: Schematic diagram showing method of preparation of patterned PS and PMMA surfaces using block-copolymer technique

in spin coater. This allows $\sim 6-7$ nm brush thick onto silicone wafer.

2. PS-PMMA block copolymer (Mn: 88k, PS = 70 vol%) is coated with 30–35 nm thickness depending on rpm of spin coater. The wafers are then additionally annealed at 170° C for $1 \sim 2$ days.

3. PMMA part of PS-PMMA block copolymer is removed with UV exposure followed by rinsing with acetic acid (AA). This step gives the surface with patterned pits in PS matrix.

4. Patterned PMMA surface (patterned pits in a PMMA matrix) is prepared by swelling the block copolymer film in acetic acid (AA), which is selectively soluble with PMMA.

Surfaces prepared using polymer spin-transfer printing

The method of preparation of nanopatterned surfaces using polymer spin-transfer printing is mentioned in detail in literature [32, 3], and it is shown in the schematic diagram in Figure 2.3.

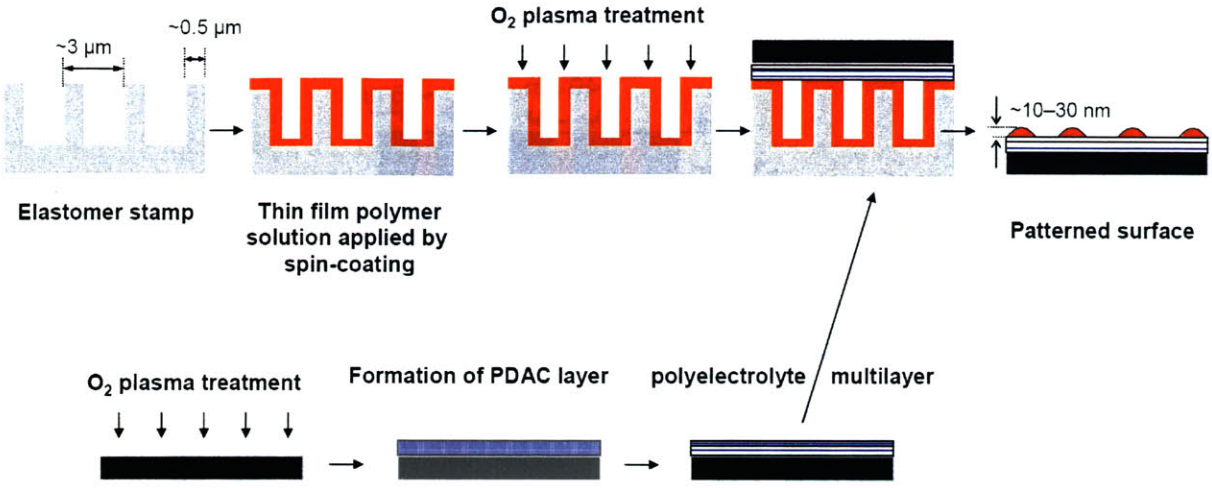

Figure 2.3: Schematic diagram showing method of preparation of dot- and stripe- patterned surfaces using polymer spin-transfer printing

The step by step procedure is as follows:

1. A very thin polymer film ($< \sim 80$ nm) is applied to polyurethaneacrylate stamp via spin-coating (2000-3000 rpm, 30s) with a 0.52 wt. % toluene solution.
2. The polymer-coated stamp is treated with O_2 plasma to generate negative charge on the polymer surface.
3. The stamp is then pressed lightly onto a positively charged substrate with poly-(diallyl dimethyl ammonium chloride) PDAC on a hot plate at 75°C; only the parts of the stamp with conformal contact with the surface are transferred in this process. The remaining regions of the surface maintain their hydrophilic, positively charged nature from the underlying layer of polycation monolayer.
4. The stamp is then peeled off the substrate while hot.

The patterns transferred are limited only by the pattern obtained in the stamp. Figure 2.4 shows few of the many stamps used to transfer the patterns using the above procedure.

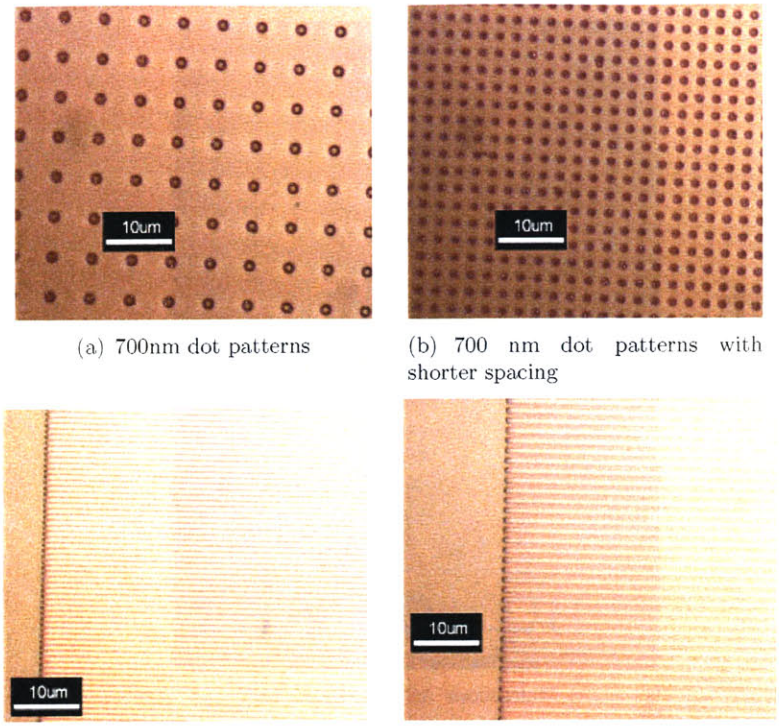

(a) 700nm dot patterns

(b) 700 nm dot patterns with shorter spacing

(c) 400 nm line patterns

(d) 700 nm line patterns

Figure 2.4: Different stamps used for transferring patterns in polymer spin-transfer printing

2.2 Instrumentation

2.2.1 Atomic force microscope (AFM)

In this study, a multi-mode Nanoscope IV atomic force microscope (AFM) from Digital Instruments is used to image the topology at liquid-surface interface. Figure 2.6(a) shows the instrument in our lab. AFM, invented in 1986 by Binnig, Quate and Gerber [12], utilizes a sharp probe (a tip on the end of a cantilever) moving over the surface of a sample in a raster scan to sense the topological changes on the surface of the sample. Figure 2.6(b) shows the schematic of the working principle of the instrument. Every variation of the surface height varies the force acting on the tip, which consequently varies the bending of the cantilever. This bending results in a change in location and intensity of the reflected laser light from the cantilever onto the split photo-diode. By measuring the difference signal in the photo-diode, changes in the bending of the cantilever can be measured.

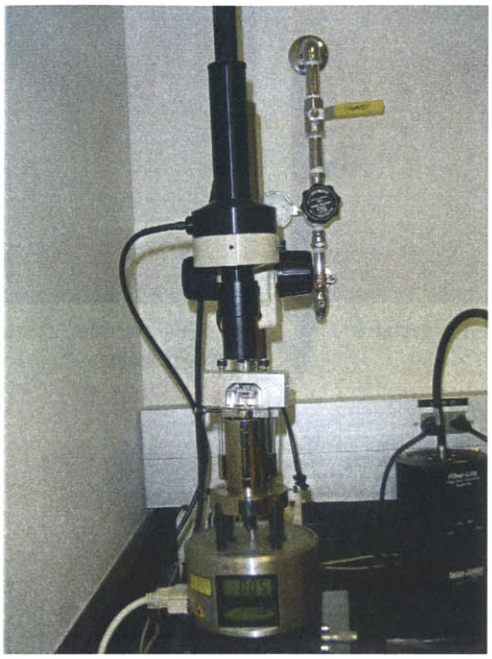

(a) Multi-mode AFM at HML, MIT

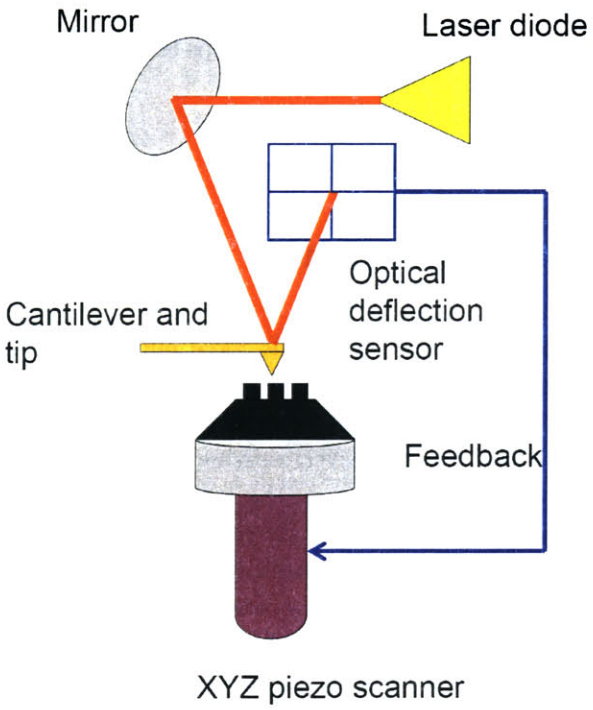

(b) Schematic of AFM

Figure 2.5: Atomic force microscope (AFM)

There are different set-ups possible for using AFM of which, two of the more common ones are used mainly in this study; these two set-ups are in-air and in-liquid, and are shown in Figure 2.6. Imaging in liquid medium is done with the help of fluid cell, which is shown in Figure 2.6(c).

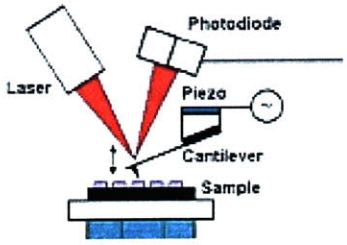

(a) In-air scanning [1]

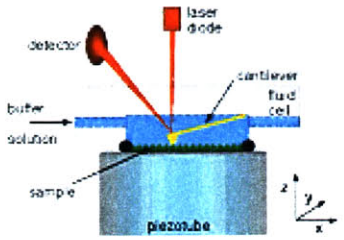

(b) In-fluid scanning with the help of fluid cell [1]

(c) Fluid cell[2]

Figure 2.6: Air and liquid mediums for AFM scanning ([1] *www.microanalytical.com*; [2] *Veeco Instruments*)

Imaging in liquid medium is particularly useful for kinds of experiments carried out in this study, where the aim is to study the topology at liquid-solid interface. Imaging in liquid medium is also useful for some of biological samples which cannot survive outside a particular liquid environment.

Besides different fluid mediums, AFM can also be operated in different modes to give various pieces of information about the surface. In this study, AFM is mainly used in tapping mode, contact mode and sometimes in friction mode.

Contact mode imaging

In contact mode of operation, the cantilever deflection under scanning reflects repulsive force acting upon the tip. Repulsion force F acting upon the tip is related to the cantilever deflection value x under Hooke's law: $F = -kx$, where k is cantilever spring constant. The spring constant value for different cantilevers usually vary from 0.01 to several N/m. The distance piezo moves to keep the cantilever deflection constant gives the height information of the surface. Schematic of working principle of contact mode imaging is shown in figure 2.7

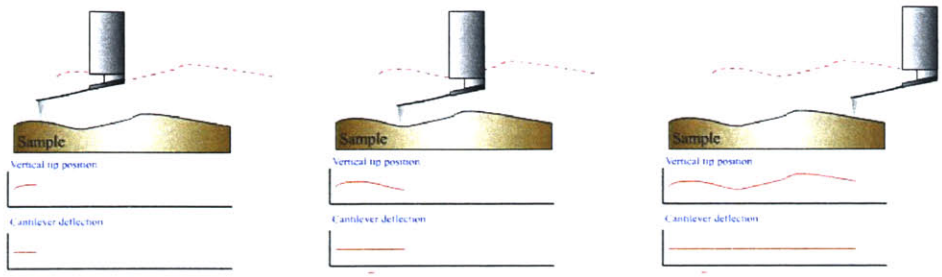

Figure 2.7: Schematic showing working principle of AFM contact-mode imaging ([1])

Friction mode imaging

Friction mode allows to distinguish areas with different friction and also to obtain edge-enhanced images of any surface. This capability may be used in conjunction with topographical images during one scan to characterize the samples more completely.

The physical basics of the frictional mode are shown in figure 2.8. When scanning in the constant force mode perpendicularly to longitudinal axis of the cantilever, besides the cantilever's deflection in the normal direction, an additional torsion bending of the cantilever occurs. It is caused by the moment of forces acting on the tip. With minor deflections, the angle of torsion is proportional to the side (lateral) force. The cantilever's torsion bending is measured by the microscope optical recording system.

When moving over a flat surface with zones of different friction factors, the angle of torsion will be changing in every new zone. This allows measuring of the local friction force. If the surface is not absolutely flat, such an interpretation is complicated. To distinguish zones of different friction and relief influence one can utilize second pass on the same line in opposite direction.

Tapping mode imaging

Tapping mode is a key advance in AFM, which allows high resolution topographic imaging of sample surfaces that are easily damaged, loosely hold to their substrate, or difficult to image by other AFM techniques. Tapping mode overcomes problems associated with friction, adhesion, electrostatic forces, and other difficulties that an plague conventional AFM scanning methods by alternately placing the tip in contact with the surface to provide high resolution and then lifting the tip off the surface to avoid dragging the tip across the surface. Figure 2.15 shows the working principle of AFM operation in tapping mode.

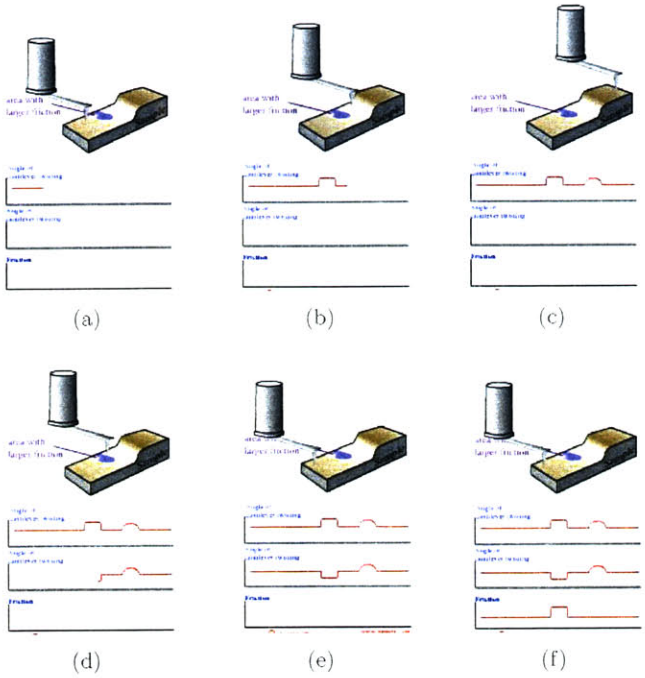

Figure 2.8: Working principle of friction-mode AFM imaging ([1])

During tapping mode operation, the cantilever oscillation amplitude is maintained constant by a feedback loop. When the tip passes over a bump in the surface, the cantilever has less room to oscillate and the amplitude of oscillation decreases. Conversely, when the tip passes over a depression, the cantilever has more room to oscillate and the amplitude increases (approaching the maximum free air amplitude). The digital feedback loop then adjusts the tip-sample separation to maintain a constant amplitude and force on the sample.

Phase imaging

A powerful extension of tapping mode AFM is phase imaging, which goes beyond simple topographical mapping to detect variations in composition, adhesion, friction, viscoelasticity, and other mechanical properties.The phase lag of the cantilever oscillation, relative to the signal sent to the cantilever's piezo driver is recorded. The phase lag is very sensitive to variations in material properties such as adhesional and viscoelasticitic properties of the sample. It can be turned on while using tapping mode AFM. The working principle is shown in figure 2.10.

Tapping mode imaging and phase imaging are especially useful for detection of nanobubbles.

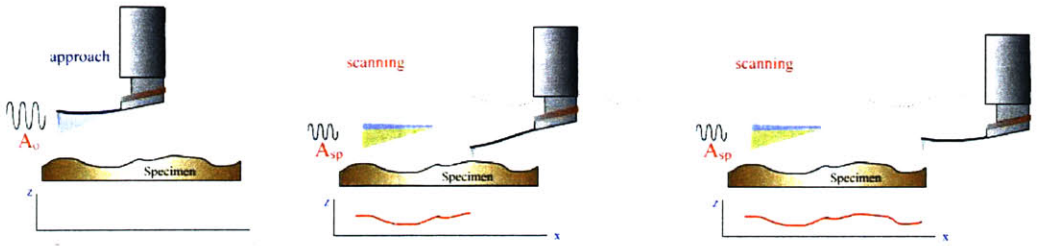

(a) (b) (c)

Figure 2.9: Schematic showing working principle of tapping-mode AFM imaging ([1])

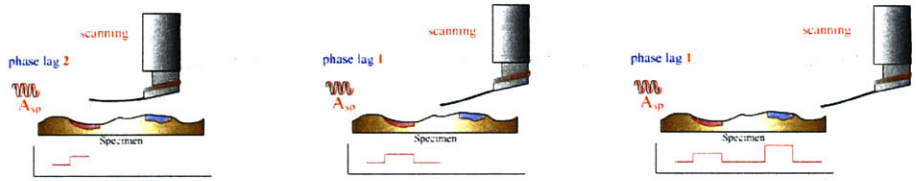

(a) (b) (c)

Figure 2.10: Phase-imaging with AFM ([1])

Since the nanobubbles are soft in nature, they would be very sensitive to force of interaction with the AFM probe. Tapping mode imaging would be therefore well suited for imaging nanobubbles as the force of interaction is much less this case. Further, since adhesional and other material properties would be significantly different at the location of bubbles from other locations, phase imaging would prove useful to detect bubbles.

Tip specification

Two kinds of tips are used in this study. Both the tips are obtained from *Veeco Instruments* and are shown in figure 2.11. Tip selection for different modes is done on the basis of recommendation by *Digital Instruments* [26]. One of them is a pyramidal shaped silicon nitride (Si_3N_4) tip (figure 2.11(a)), which is used for contact mode imaging in air and in water as well as tapping mode imaging in water. The end radius of this tip is $\sim$ 15 nm where as the spring constant is $\sim$0.15 N/m. Resonant frequency of the cantilever is $\sim$ 24 kHz in air and $\sim$ 9 kHz in water.

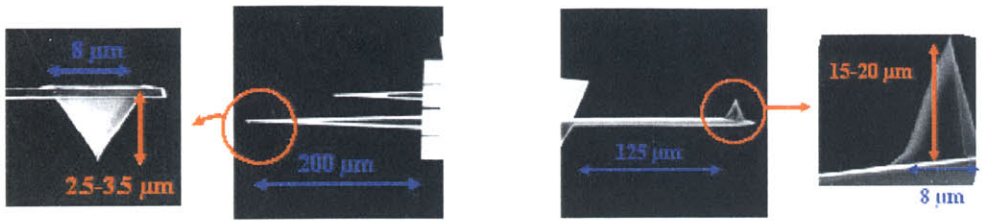

(a) Silicon nitride (Si_3N_4) probe

(b) Silicon (Si) tip

Figure 2.11: Contact-mode and tapping-mode AFM probes (*Veeco Instruments*)

For tapping mode imaging in air, a stiffer crystal silicon probe is used which is shown in figure 2.11(b). The end radius of this tip is < 10nm where as the spring constant is ~ 40 N/m. Resonant frequency of the cantilever is ~ 300 kHz in air.

2.2.2 Calibration results

To make sure the instrument is working fine and to develop a set of useful post-processing tools, a platinum coated silicon calibration sample from *Digital Instruments* is first imaged using AFM in different modes. Figure 2.12 shows the picture of the calibration sample taken by scanning electron microscope (SEM). The pitch of the pits is 10μm both in x- and y- direction. The depth of the pits is ~200 nm.

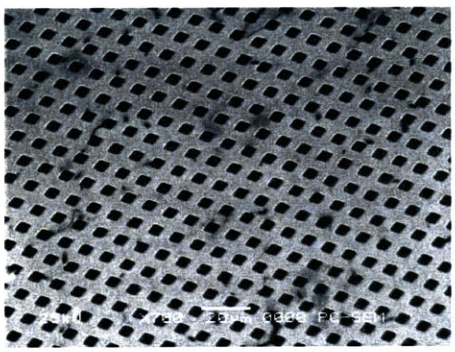

Figure 2.12: SEM picture of the calibration sample

Contact mode imaging in air

Figure 2.13(a) shows the contact mode AFM height and deflection images of the calibration

sample in air. Deflection signal is the error signal, which is used as a feedback to the piezo. When plotted, deflection signal can give an edge-enhanced image of the sample.

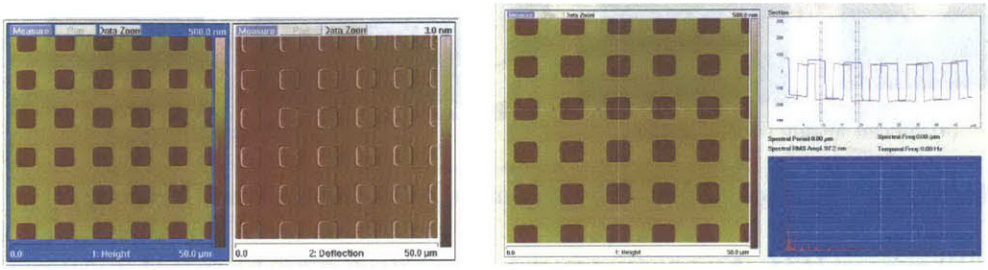

(a) Height and deflection

(b) Section analysis of the height image

Figure 2.13: Contact-mode AFM height and deflection images of calibration sample before post-processing

The height image shows the regular arrangement of square pits with uniform pitch and depth. However, a closer look at the image in figure 2.13(a) suggests that the image needs some post-processing. Height image in figure 2.13(a) shows that background is not uniform, and it consists of some dark and light patches. This fact is also revealed in the x- and y-section profile of the height image(figure 2.13(b)), where the height profiles across the lines in the x- and y- direction are not overlapping perfectly, also indicating some curvature in the background.

This problem of curvature in the background is rectified by using *flatten* command in the *modify* menu of the Nanoscope software version 5.12. The Flatten command eliminates unwanted features from scan lines. It uses all unmasked (stopbanded) portions of scan lines to calculate individual least-squares fit polynomials. The polynomials are then subtracted from each line.

This kind of analysis would be useful for samples that have sporadic, tall features in predominantly flat areas just like the calibration sample. Further, since the homogenous samples used in the present study are atomically flat with expected medium sized features randomly distributed over them in water, flattening would be useful then to remove artifacts from background. Only featureless area of the scan should be used to calculate the polynomial. Figure 2.14(a) shows an image post-flattening with few of the features (pits) not inside stopbands.

After flattening, the image is passed through a low pass filter where each data point in the image gets replaced with the weighted average of the 3x3 cell of points surrounding and including the point. Figure 2.14(b) shows the section profile across two lines in the post-

(a) Height image after flattening with only few stopbands at certain locations

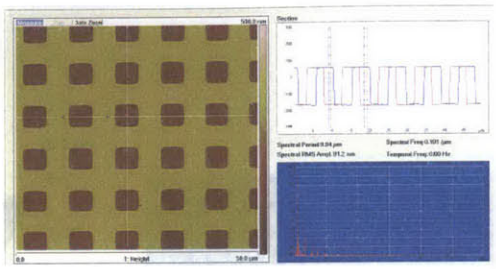

(b) Section analysis of the height image post- flattening and lowpass filtering

Figure 2.14: Flattened and lowpass-filtered images of calibration sample from AFM contact mode imaging in air

processed image. One can see that the background looks uniformly flat with overlapping blue and red lines in section profile. The height of the posts is ~200 nm and the pitch is $\sim 10\mu$m.

Tapping mode imaging in air

Similar results as above are obtained with tapping mode in air. The silicon tip was oscillated near its resonant frequency which was determined in-situ to be ~270 kHz. Figure 2.15(a) shows the post-processed (same procedure as in contact mode imaging) height and phase image obtained by tapping mode AFM of the same sample.

Figure 2.15(b) shows the 3D view of the calibration sample produced from the AFM images. The image looks like a replica of the original sample (figure 2.12). In-water imaging was not performed to save the calibration sample from getting contaminated.

2.2.3 Other instruments

A video contact angle system (VCA 2000) from *AST Products, Inc* shown in figure 2.16(a) is used to measure the static contact angle of liquid on surface. A *Kruss* K-10 tensiometer shown in figure 2.16(b), located in our lab is used to carry out surface tension measurements of different liquids used in the study.

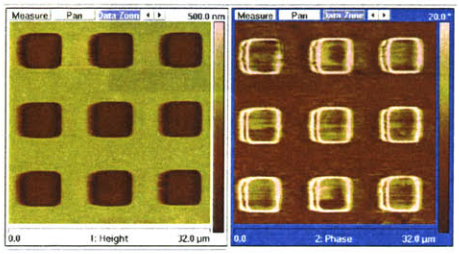

(a) Height and phase images in tapping mode

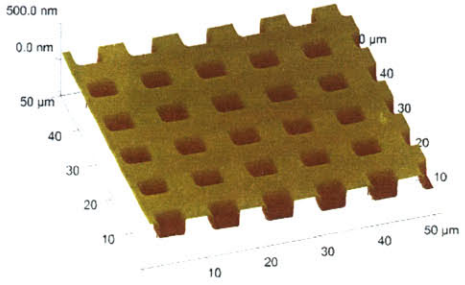

(b) 3D view generated from AFM image

Figure 2.15: In-air tapping mode AFM height and phase images of the calibration sample along with a 3D view of the same

(a) VCA 2000 dynamic contact angle system, MIT

(b) Kruss K10 tensiometer at HML, MIT

Figure 2.16: Instruments for measuring contact angle and surface tension

Chapter 3

Tests with homogenous surfaces

IN this chapter, results from experiments with various homogenous surfaces with different hydrophobicities are presented.

3.1 Polymethylmethacrylate (PMMA) surfaces

As mentioned in chapter 2, polymethylmethacrylate (PMMA) surfaces give a contact angle value of $\sim 72^{o}$ with water (figure 3.1(a)), which suggests that PMMA surfaces are more hydrophilic in nature than hydrophobic. Figure 3.1(b) shows the contact mode AFM height and deflection images of the sample surface in air. The images are featureless and reveal no other information besides the surface being very smooth.

Two parameters are defined hereafter for most of the AFM images to get an idea about the roughness level of the sample surface in the image. One of them is root mean square roughness (R), which is defined as following:

$$R = \sqrt{\frac{\sum Z_i^2}{N}} \tag{3.1}$$

where Z_i is the height deviation taken from the mean image data plane; N is the number of data points. The second parameter is $R_{\max}$, which is defined as the maximum vertical distance between the highest and lowest data points in the image.

For the height image in figure 3.1(b), the RMS roughness, $R = 0.273$ nm, and $R_{\max} = 2.2$ nm. These values suggest that the surface is atomically smooth. Figure 3.2 shows the tapping mode AFM height and deflection images of PMMA surface in water. One can see that the images are again featureless and not very different compared to ones taken in air. The roughness values in the height image in figure 3.2 are $R = 0.50$ nm and $R_{\max} = 4.2$ nm. Though these values are slightly higher than the values corresponding to in-air height image, there is no significant difference in between the two sets. Thus, in conclusion to the

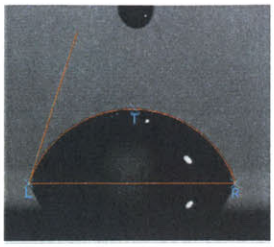

(a) $\theta \sim 72^{\circ}$

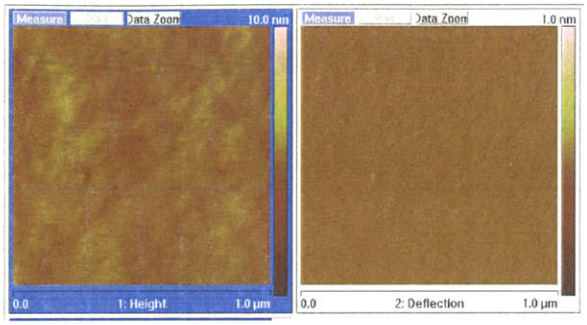

(b) Height and deflection images ($R = 0.273$ nm; $R_{\max} = 2.2$ nm)

Figure 3.1: PMMA surface: contact angle with water and in-air AFM contact mode height and deflection images

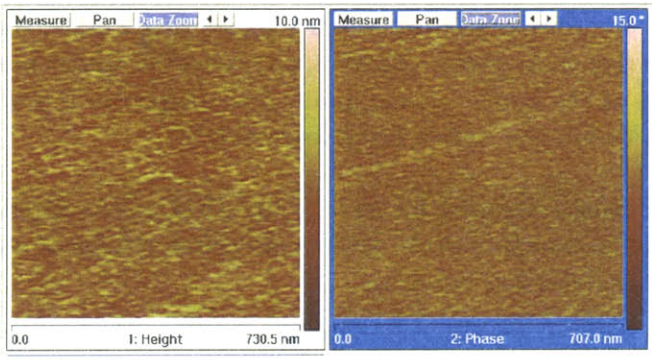

Figure 3.2: Tapping mode AFM height and phase images of PMMA surface in water ($R = 0.50$ nm; $R_{\max} = 4.2$ nm)

experiments with PMMA surface, we can say that the surface topology remains unchanged in water.

3.2 Polystyrene (PS) surfaces

Next surface which is studied in this section is plain polystyrene (PS) surface. The method of preparation of these surfaces are given in detail in chapter 2. PS surfaces give a contact angle value of $\sim 97^{\circ}$ with water (figure 3.3(a)). This suggests that PS surfaces are fairly

hydrophobic. Figure 3.3(b) shows the contact mode AFM height and deflection images

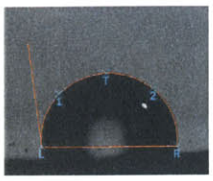

(a) $\theta \sim 97°$

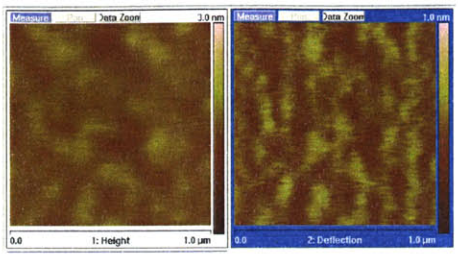

(b) Height and deflection images ($R = 0.125$ nm; $R_{\max} = 0.86$ nm)

Figure 3.3: PS: contact angle with water and in-air contact mode AFM height and deflection images

of the sample surface in air. The images look featureless and reveal no other information besides the surface being very smooth. The roughness values for the height image are $R = 0.125$ nm and $R_{\max} = 0.86$ nm. This again tells us that the surface is atomically smooth.

Figure 3.4 shows the tapping mode AFM height and phase images of the sample in water. Unlike PMMA surface, this time the image looks quite different to one taken in air.

The roughness values for the height image in this case are $R = 1.1$ nm and $R_{\max} = 12$ nm. These values are an order of magnitude higher than the values for the height image in air. One can notice that images in-water are not featureless like the in-air images but instead show randomly distributed, uniformly spread domains. Further, the features appear together in phase as well as height image which suggests that besides topological difference, there is also some difference in material properties at these locations. Let us see some more evidences before we start calling them *nanobubbles*.

Figure 3.5(a) shows an AFM scan of larger surface area ($100\ \mu m^2$) under the same conditions as above. One can see that the features are distributed all over the area and are not localized to any region in any sense. Figure 3.5(b) shows a 3-D view of the surface covered with these features in water. This figure suggests that such a surface can no longer be assumed to be smooth in water.

Figure 3.6 shows the height and phase profile along the cross-sections of these features. In figure 3.6(a) it can be seen that the shape of these features is that of symmetric lobes having a smooth profile. The height of the features is $\sim \mathrm{O}\,(5 - 10\,\mathrm{nm})$ and width is $\sim \mathrm{O}\,(100 - 150\,\mathrm{nm})$.

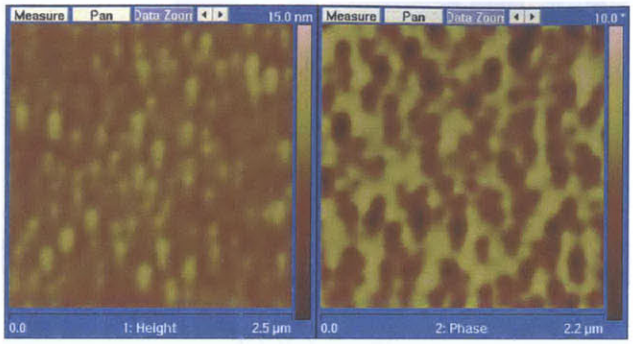

Figure 3.4: Tapping mode AFM height and phase images of the PS surface in water ($R = 1.1$ nm; $R_{max} = 12$ nm)

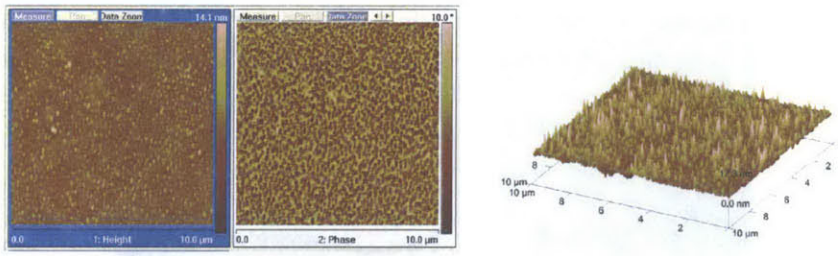

(a) A scan over 100 μm^2 (b) 3-D view

Figure 3.5: 3-D view of nanobubbles distributed over a large area on PS surface

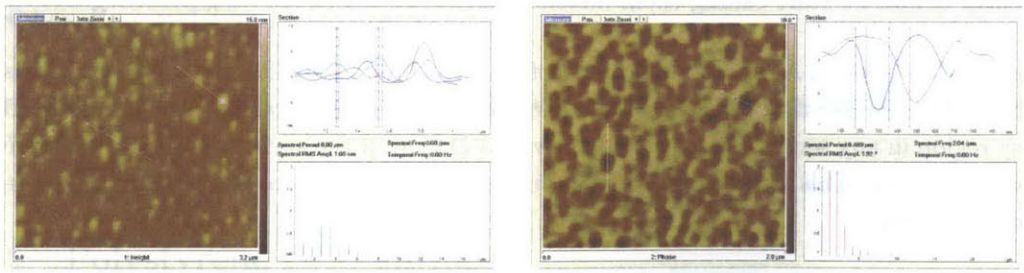

(a) Height cross-section profile (b) Phase cross-section profile

Figure 3.6: Height and phase profile along the cross-sections of few nanobubbles on PS surface

Figure 3.6(b) also shows a systematic phase angle drop that is going all the way from the rim to the center of the individual bubbles. This can be attributed to a stabilization of the rim shape that is induced by the surface tension itself. Even a small mechanical deformation by interaction with the tip would be equivalent to a shape change along the rim; i.e. it would need to work against the interfacial energy, requiring a force higher than what is necessary for a small deformation of a gas volume that takes place far away from the rim. The phase variation thus indicates the presence of extended gas bubbles that respond with varying compressibility as the tip probes their surfaces.

Variation in images with different interaction force

So far, the AFM images presented in this study have been either contact mode in-air images or tapping mode in-water images. An interesting question at this point could be that what would we see if we were to carry out a contact mode imaging in water. To get an answer to this, let us see the effect of varying force of interaction between the AFM probe and the sample surface in tapping mode itself.

Figure 3.7 shows the effect on images upon varying the tapping force while scanning. Before we look into the individual images in the figure, there are two things to keep in mind. First, the tapping force while scanning is varied by changing the "setpoint voltage" in the online menu, and second, higher the value of the setpoint voltage, the lower would be the magnitude of tapping force.

Figure 3.7(a) is obtained by scanning with setpoint voltage set as 1.2 V and is the same image as shown in figure 3.5(a). The force is then increased by decreasing the setpoint voltage to 0.9 V. The image corresponding to this setpoint voltage is shown in figure 3.7(b). The image still shows nanobubbles distributed in the same way as before on the surface. However, the roughness value has changed slightly in the height image and significantly in the phase image. This observation suggests that the slight increase in the tip-sample interaction force in this case resulted in increased sensitivity and better tracking of the surface features by the probe.

Decreasing the setpoint voltage further to 0.6 V results in a still higher value of tapping force. The image is featureless corresponding to this voltage. After scanning at this setting for one complete scan, the setpoint voltage is switched back to 0.9 V. Figure 3.7(c) shows the image obtained using this setting. One can see that the image looks quite different to the one in figure 3.7(b), which was also taken with setpoint voltage set as 0.9 V. Large-sized but less-frequent features are observed which suggest that the features might have gotten affected by the strong interaction with the tip. This observation strengthens the fact that these features are fragile bubbles which get coalesced to form large bubbles upon being

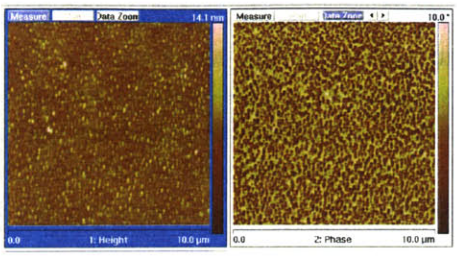

(a) 1.2 V as setpoint voltage (R = 1.1 nm (height), 1.91° (phase))

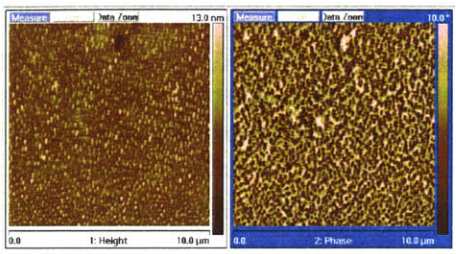

(b) 0.9 V as setpoint voltage (R = 1.6 nm (height), 21° (phase))

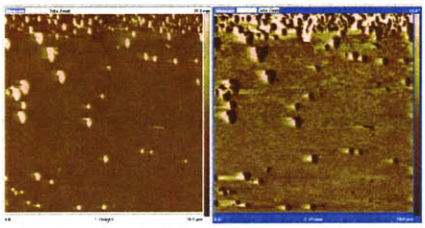

(c) Back to 0.9 V as setpoint voltage after scanning once at 0.6 V (with 0.6V, image was featureless)

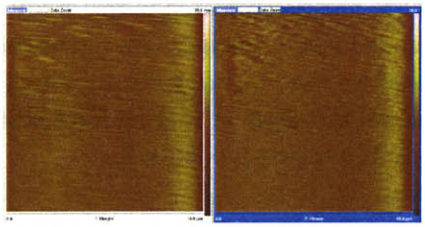

(d) 0.4 V as setpoint voltage

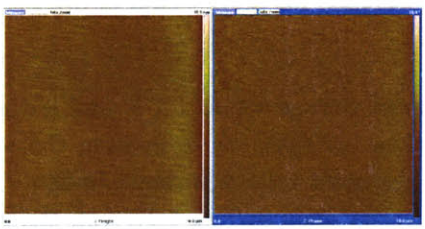

(e) Back to 0.9 V setpoint voltage after scanning once at 0.4 V

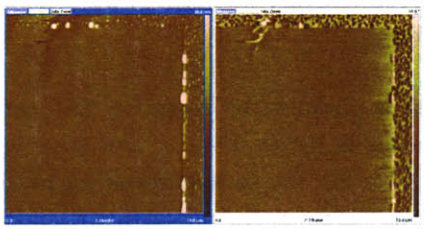

(f) 1.2 V as setpoint voltage (8 minutes into re-engagement after disengaging)

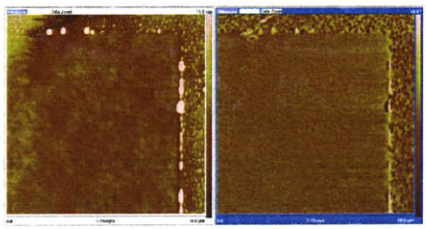

(g) 1.2 V as setpoint voltage (~ 20 minutes into re-engagement)

Figure 3.7: Variation in tapping mode AFM images (of PS in water) with different tapping force

displaced from their original location.

Upon decreasing the setpoint voltage further to 0.4 V, the image gets featureless (figure 3.7(d)). Furthermore, this time upon switching back to 0.9 V, the image remains featureless (figure 3.7(e)). This observation suggests that upon much harder tapping, bubble can also get scrapped off from the surface completely.

At this point, the tip is disengaged and scanning is stopped. Upon engaging the tip again after a few minutes, sample surface looks like figure 3.7(f). The area which was scanned earlier still remains featureless while the area around the periphery of the scanned area show the originally features. Figure 3.7(g) shows the surface topology after 20 minutes into re-engagement. The scraped off area is still featureless while the region around the periphery of the featureless area exhibits features similar to those observed in the original images with 0.9 V as setpoint voltage.

The above experimental results give strong evidences in confirmation of the features being soft and fragile domains which can be easily manipulated by the tip. The only possibility then is that these features are essentially air pockets, and hence, hereafter these features are dubbed as nanobubbles.

3.3 Silicon surfaces hydrophobized with octadecyltrichlorosilane (OTS)

Next surface which is used in this section is hydrophobized silicon with octadecyltrichlorosilane (OTS). The method of preparation of this surface is discussed in detail in chapter 2. Hydrophobized silicon surface with OTS gives a contact angle value of $\sim 110^{o}$ with water (figure 3.8(a)). This suggests that this surface is even more hydrophobic than polystyrene, which has the contact angle value of $\sim 100^{o}$ with water.

Figure 3.8(b) shows the tapping mode AFM height and phase images of the sample in ethanol. The images look featureless and reveal no other information besides the surface being very smooth. The roughness values for the height image are $R = 0.285$ nm and $R_{max} = 3$ nm, which suggest that the surface is atomically smooth. On a different note, we can also infer from these images that nanobubbles don't appear on surfaces in ethanol medium. This observation seems reasonable if we consider the contact angle of ethanol on this surface ($\sim 30^{o}$), which is too low for this surface to be lyophobic.

Figure 3.9(a) shows the tapping mode AFM height and phase images the surface in water.

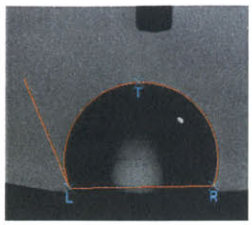

(a) $\theta \sim 110^{o}$

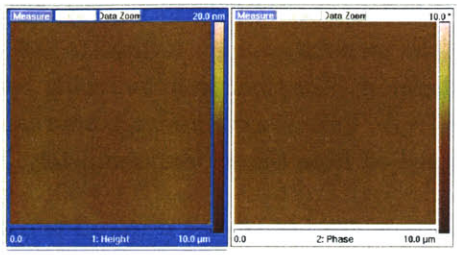

(b) Height and phase images ($R = 0.285$ nm; $R_{\max} = 3$ nm)

Figure 3.8: Contact angle with water and tapping mode images of OTS hydrophobized silicon surface in ethanol

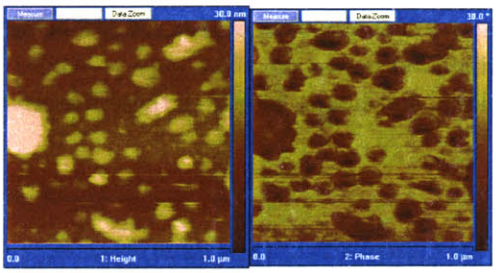

(a) $1\mu m^2$scan area ($R = 5$ nm; $R_{\max} = 44$ nm)

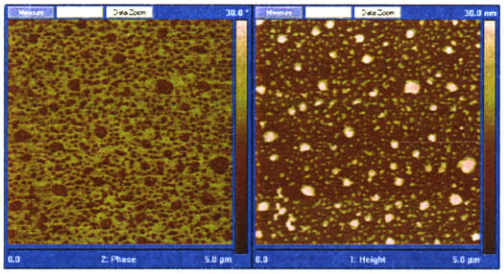

(b) $25\mu m^2$scan area($R = 4.5$ nm; $R_{\max} = 52$ nm)

Figure 3.9: Tapping mode AFM height and phase images of OTS hydrophobized silicon surface in water

The images look very different from the images in case of ethanol. Randomly distributed features appear in both height as well as phase images. Phase images also show a distinct contrast which suggests that the material properties are different from that of background surface. The roughness values in the height image are $R = 5$ nm and $R_{\max} = 44$ nm. These values are significantly higher than the roughness values of the height image in air and in ethanol. Other observations like disappearance of these features upon harder tapping etc are similar to the observations made in the case of polystyrene surface. Figure 3.9(b) shows an image of a larger scan area of the sample surface under the same conditions as above. The image shows that bubbles are spread uniformly over the whole surface and not localized to one particular region. From the cross-section profile across the nanobubbles, the height of the bubbles is found to be $\sim$ O(15nm) where as the width is found to be $\sim$ O (200nm). These values are higher than the values obtained for nanobubbles on polystyrene surfaces in earlier section. Detailed calculations of different bubble parameters on these surfaces are

done in chapter 5.

3.4 Rough glass surfaces hydrophobized with octadecyltrichlorosilane (OTS)

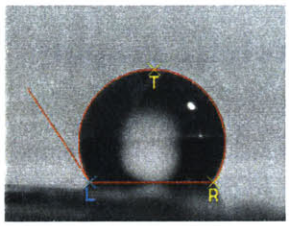

(a) $\theta \sim 120^{o}$

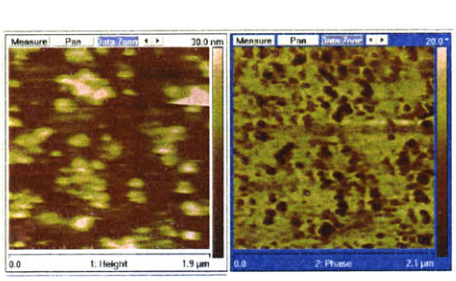

(b) $4\mu m^2$ scan area (R = 3.3 nm, R_{max} = 22 nm)

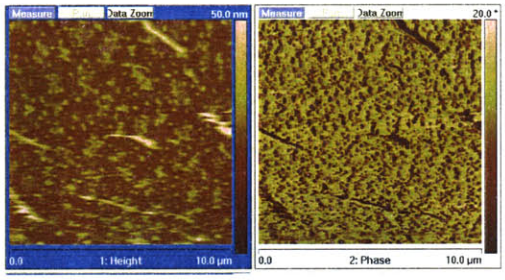

(c) $100\,\mu m^2$ scan area (R = 4.8nm; R_{max} = 58.7 nm)

Figure 3.10: In-water tapping mode AFM height and phase images of rough glass surface hydrophobized with OTS

Next sample which is discussed in this section is rough glass wafers hydrophobized with octadecyltrichlorosilane (OTS). This sample gives a contact angle of $\sim 120^{o}$ as shown in figure 3.10(a). Since the chemistry of the exposed surface depends on the hydrophobizing agent (in this case OTS) and not on the underlying substrate, a higher contact angle value compared to the value with OTS hydrophobized silicon seems unreasonable. However, in the above statement topological effects or roughness effects of the sample on the contact angle is not taken into account. For glass wafers which are thoroughly cleaned after hydrophobization to make sure all the silane is rinsed off, the contact value is still $\sim 110^{o}$ similar to value obtained for OTS hydrophobized silicon surface. However, for the case when the glass wafers are cleaned with ethanol before chloroform, the contact angle observed is higher and around 120^{o}. The reason behind this observation can be silane (not rinsed off completely) polymerizing in presence of water present in impure ethanol.

Carrying out the AFM experiments with both kinds of wafers results in similar picture to that of OTS hydrophobized silicon. The in-water tapping mode AFM images show nanobubbles sitting all over the surface. Figure 3.9(a) shows the AFM image corresponding to the hydrophobized rough glass wafers. From the cross-section profile across the nanobubbles, the height of the bubbles is found to be $\sim$ O(20nm) where as the width is found to be $\sim$ O (220nm).

3.5 Highly oriented pyrolytic graphite (HOPG) surfaces

In this section experimental results using highly oriented pyrolytic graphite (HOPG) is presented. One of the reasons why HOPG surface is interesting to study is that it gives a contact angle value of $\sim 90^{o}$ with water(figure 3.11(a)), which puts this surface in the middle of hydrophilic and hydrophobic regimes.

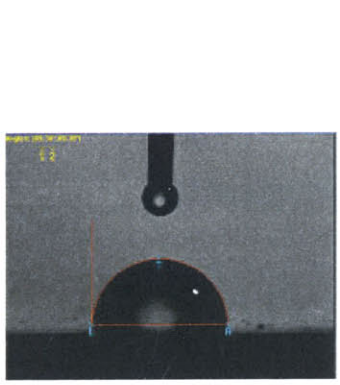

(a) $\theta \sim 90^{o}$

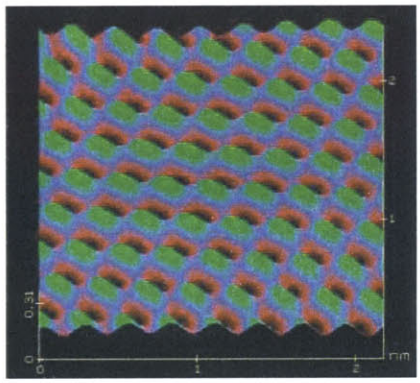

(b) Individual carbon atoms imaged on a HOPG surface using AFM (*nanomechanicslab@MIT*)

Figure 3.11: Contact angle with water and an AFM image showing individual carbon atoms on a HOPG surface

Figure 3.12 shows the tapping mode AFM height and phase images of HOPG in water. The images are featureless with an odd appearance of features in between steps. However, these features are not nanobubbles as they remain in the image even upon harder tapping. The roughness values for the height image are $R = 0.3$ nm and $R_{\max} = 3.3$ nm which are quite low indicating the surface is atomically smooth even in water.

However, one of the research groups studying nanobubbles, Lou *et* al. [36, 37, 63], report to

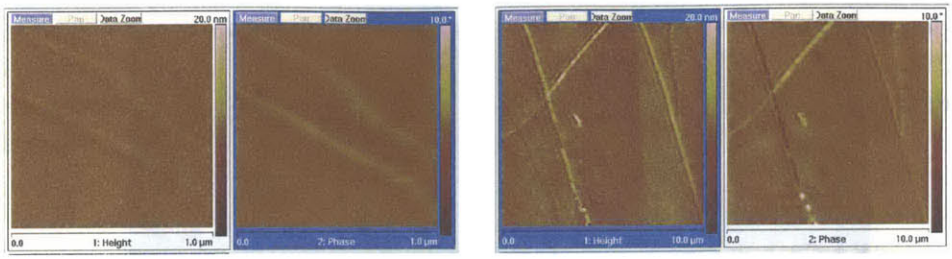

(a) Featureless surface (R = 0.3 nm; R_{max} = 3.3 nm)

(b) With odd features in between the steps (R = 1.3nm; R_{max} = 35.7 nm)

Figure 3.12: Tapping mode AFM height and phase images of HOPG in water

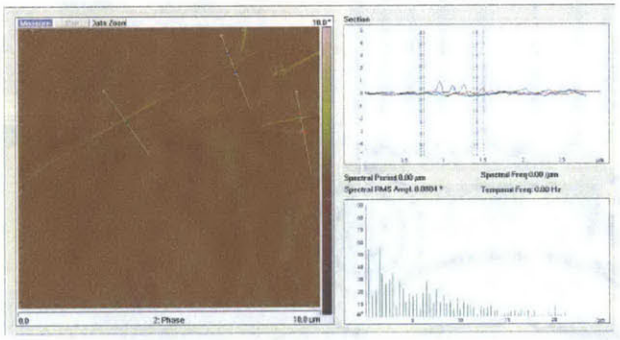

Figure 3.13: Atomic steps seen in tapping mode AFM height image of HOPG in ethanol

have seen nanobubbles on HOPG surfaces following a different experimental procedure from the one taken here. At first, they inject ethanol into the fluid cell. After some time, they replace ethanol in the fluid cell with water. Upon imaging then, they see huge nanobubble sitting on the surface.

Following the same procedure here, ethanol is first injected into the fluid cell of AFM. Figure 3.13 shows the image of the HOPG sample in ethanol. No features are observed in this case. In fact, surface is smooth enough to give the jump in height at the atomic steps as $\sim$ 1 nm.

Continuing with the procedure given by Lou *et* al., water is injected replacing ethanol in the fluid cell. Figure 3.14 shows the AFM image taken at this stage. The image still appears to be featureless which is not in agreement with the observation made by Lou *et* al. The

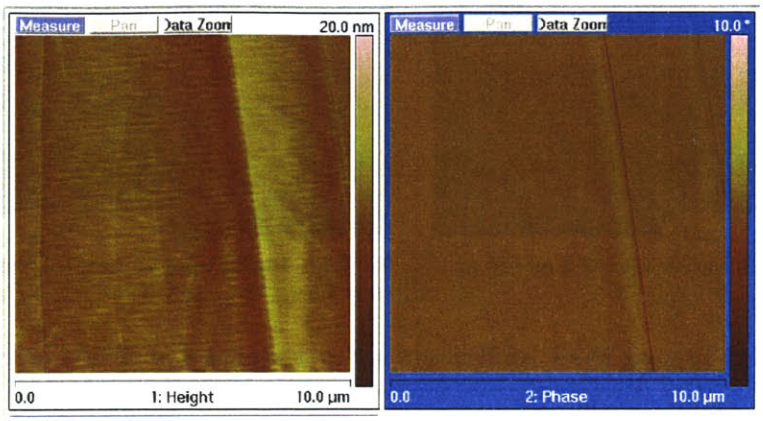

Figure 3.14: HOPG in water just when ethanol is flushed out

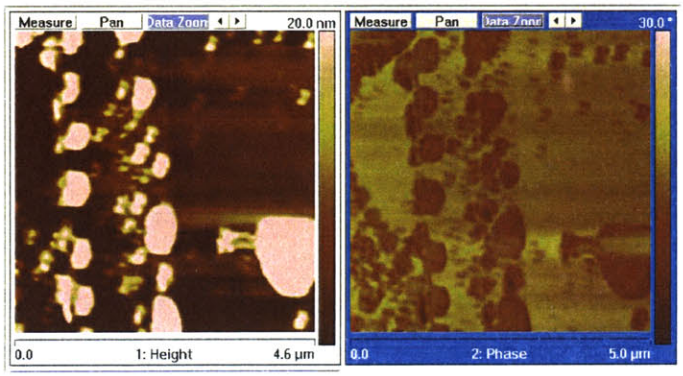

Figure 3.15: HOPG surface in water after ethanol is completely flushed out and enough water is flushed in

values of roughness parameters (R = 0.3 nm; $R_{\max}$ = 3.3 nm) further indicate that the surface is still atomically smooth.

Figure 3.15 shows the image after injecting water for a longer time and then waiting for $\sim$ 15 minutes. The picture looks very different from figure 3.14. Large round features appear both in height as well as phase image. Similar characteristics to nanobubbles are observed for these features e.g. consistent round shapes, high contrast in phase image at the location of these features, disappearance upon harder tapping.

Further, bubbles seem to be aligned along a line in the image. This line could very well be

the atomic step which is providing a energy favorable site for these bubbles to grow. Taking a cross-section across these bubbles as shown in figure 3.16(a) gives the diameter of these bubbles to be of the order of 1 μm and the height to be around the order of 50 nm. These observations are similar to that made by Lou *et* al. [37]. Figure 3.16(b) shows the picture of nanobubbles on HOPG surface obtained by them.

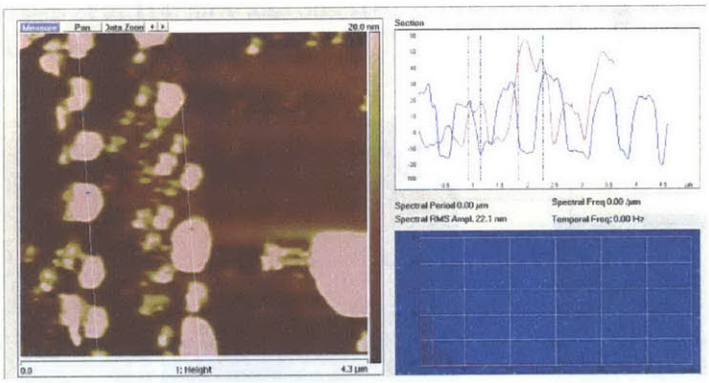

(a) Height profile along a cross-section of nanobubbles

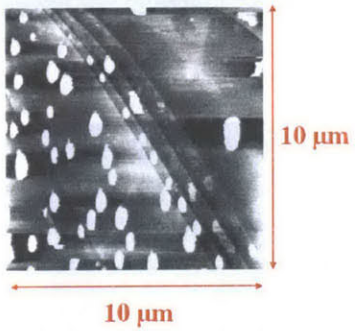

(b) HOPG in water Lou *et* al. ([36, 37])

Figure 3.16: Cross-section profile of nanobubbles on HOPG

Here, we can notice a difference in mechanisms of formation of nanobubbles on HOPG and the previous hydrophobic surfaces. While in the case of PS, and silane hydrophobized silicon and glass wafers, bubbles formed instantly in water, in the case of HOPG they do not form instantly on water. As found, nanobubbles only form on HOPG surface after the exchange of fluid from ethanol to water inside the fluid cell. This observation suggests that the nanobubble formation in the case of HOPG surface is not because of any thermodynamic reason but is rather due to solubility effect. This reasoning makes more sense if we take a look at the graph in figure 3.17 which plots solubility of different gases against ethanol %

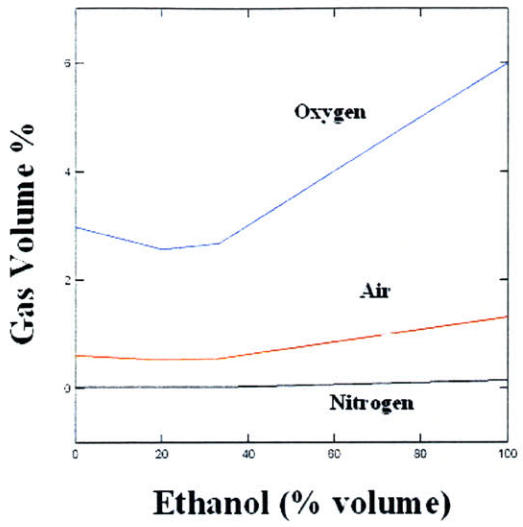

Figure 3.17: Solubility of different gases versus ethanol % in a solution of ethanol and water

in ethanol-water mixture.

This graph can help explain the origin of nanobubbles appearing after injection of ethanol followed by water. Since the solubility of air (and more so, oxygen) is greater in ethanol than water, and moreover, the surface does not *hate* ethanol as much as it does water, undissolved air in ethanol may possibly come out to form nanobubbles when fluid cell is flushed with water.

3.6 Experiments with ethanol as the solvent liquid

So far, nanobubbles have been observed on different homogenous hydrophobic surfaces in water. It would be interesting to see what effect does changing the fluid over the surface have on nanobubble formation. Earlier in this chapter, for the case of OTS hydrophobized silicon, we saw that no nanobubbles were observed with ethanol as the solvent. This suggests that surfaces that are hydrophobic enough to support bubble formation may not be lyophobic enough to support bubble formation in less polar solvent medium. The reason behind the above phenomena is the lower surface tension value of ethanol ($\sim$23 mN/m) as compared to that of water ($\sim$72 mN/m).

Figures 3.18 and 3.19 show a typical sequence when water in the fluid cell is replaced by ethanol. The sample in this case is plain polystyrene surface. With water in the fluid cell, a surface uniformly covered by nanobubbles is seen (figure 3.18(a)). Upon flushing ethanol, often microbubbles are observed which originate in-situ and can be seen in the microscope attached to the AFM (figure 3.18(b)). The reason behind formation of these microbubbles could be the solubility difference of the gas in ethanol and water as described in the previous section. Carambassis *et* al. [14] have also observed formation of microbubbles upon changing the electrolyte in their experiments.

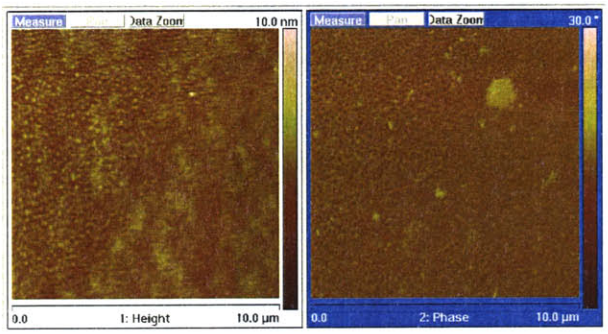

(a) Nanobubbles on PS surface in water

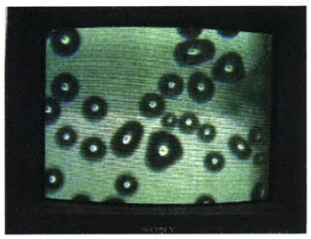

(b) Microbubbles observed in microscope upon injection of ethanol in fluid cell

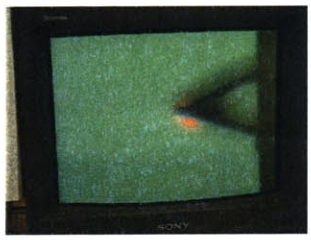

(c) Clear location amidst microbubbles for AFM scanning

Figure 3.18: Sequence of images of polystyrene surface upon change in liquid in fluid cell

In this configuration, imaging with AFM is not possible as the bubbles present near tip interfere with the tip-sample interaction. However, upon injecting more ethanol into the fluid cell to flush out the microbubbles, there would be usually some locations where bubbles are less frequent and imaging is possible. Such a location is shown in figure 3.18(c). The AFM image itself at this location is shown in figure 3.19(a). In the AFM image, one can see dark patches in the height image which suggests that tip is bursting the bubbles as it comes down upon it. Similarly, no contrast is seen in the phase image corresponding to the dark regions in the height image. Upon flushing more ethanol, surface shows no sign of

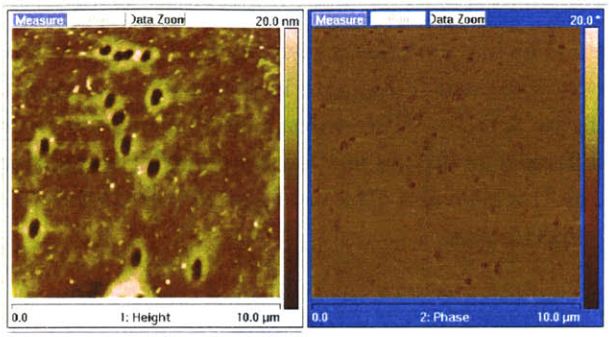

(a) AFM image showing large bubbles on PS surface upon changing the liquid in fluid cell

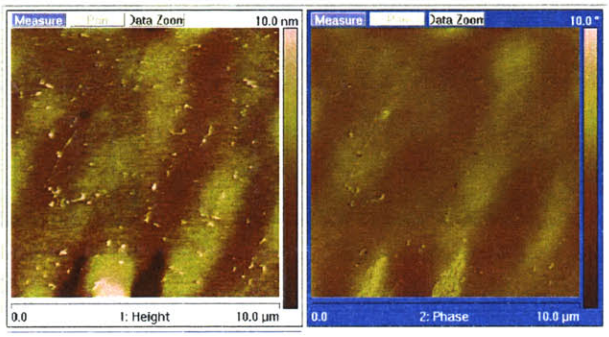

(b) Featureless PS surface upon flushing more ethanol in

Figure 3.19: Sequence continued from figure 3.18

bubbles as shown in figure 3.19(b) which is consistent with the rest of observations.

Figure 3.20 shows the area % of nanobubbles with amount of ethanol in a solution of ethanol and water. We can see that the area of nanobubbles decreases very rapidly with ethanol content.

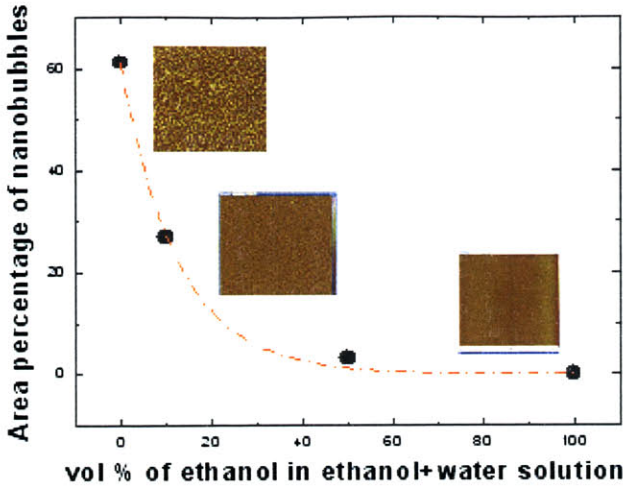

Figure 3.20: Area fraction of nanobubbles with percentage of ethanol in solution of ethanol and water

Ethanol vol.% in solution	Surface tension, γ_{lv} (mN/m)	Contact angle on PS, θ (degrees)
0	72	100
10	54	99
25	41	86
50	29	67
75	26	58
100	23	42

Table 3.1: Surface tension and contact angle values for ethanol-water solution with different composition

As mentioned earlier, the decreasing area percentage of nanobubbles on polystyrene surface with increasing ethanol % in ethanol-water solution is due to the low surface tension of value of ethanol. Table 3.1 lists the surface tension and contact angle values (on polystyrene) of ethanol-water solutions with different volume percentage of ethanol.

Further, figure 3.21 shows the variation in $\cos(\theta)$ against inverse of surface tension for data in table 3.1. The curve is not linear, but can be approximated by a straight line as a first order approximation. This is in accordance with the Young's equation (equation 3.2) which

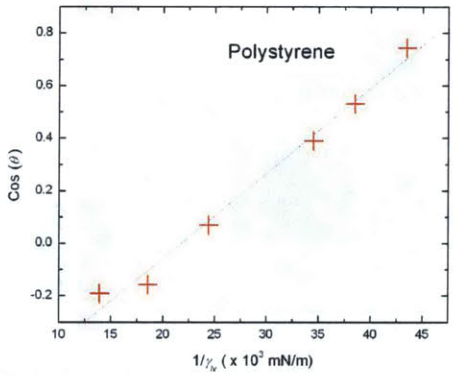

Figure 3.21: Contact angle (on polystyrene surface) against surface tension for ethanol-water solution

relates these two quantities.

$$cos(\theta) = \frac{\gamma_{sv} - \gamma_{sl}}{\gamma_{lv}} \tag{3.2}$$

Chapter 4

Tests with nanopatterned surfaces

ONE of the conclusions that can be drawn from the experiments with homogenous surfaces in chapter 3 is that nanobubbles are selective in their occurrence. While they exist on mostly hydrophobic surfaces, they are not present on hydrophilic surfaces. This observation suggests a possibility of controlling the distribution, number and size of nanobubbles by using surfaces consisting of patterns of nanoscale hydrophobic sites in a hydrophilic matrix and vice-versa.

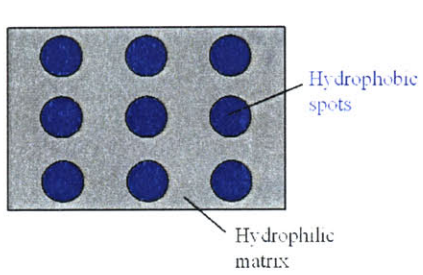

(a) Dot patterned surface

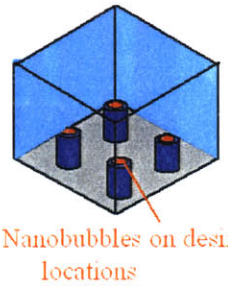

(b) Schematic of presence of nanobubbles on only the hydrophobic sites

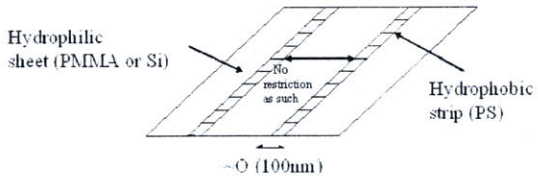

(c) Lamellae pattern

Figure 4.1: Schematic diagram of nanopatterned surfaces which can be used to control the location and extent of nanobubbles

Controlling the extent of nanobubbles is desirable as that would in turn give a control over macroscale frictional properties. Figure 4.1 illustrates the above idea where nanopatterned

surfaces (with either dot or lamellae patterns) can be used to control the location and extent of nanobubbles. In the subsequent sections of this chapter, experimental results with different sets of nanopatterned surfaces are presented.

4.1 Nanopatterned surfaces prepared using block-copolymers

Experiments with two sets of nanopatterned surfaces - patterned polymethylmethacrylate (PMMA) and patterned polystyrene (PS) - are discussed in this section. These surfaces were prepared using block-copolymers and were provided to us by Prof. T. Russell's research group at UMass. Amherst. The method of preparation is discussed in detail in chapter 2.

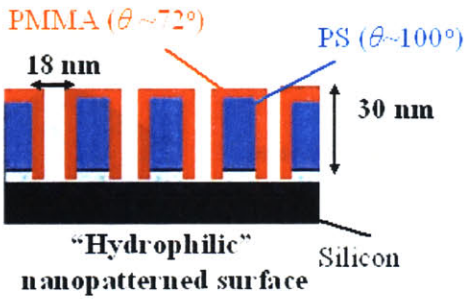

(a) Schematic of the sample

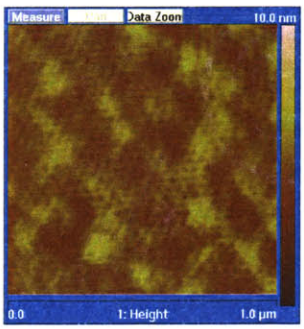

(b) Contact mode AFM height image of sample in air (R = 0.65 nm; R_{max} = 4.8 nm)

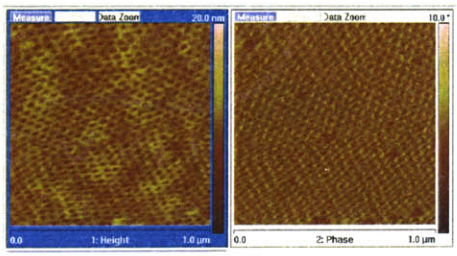

(c) Tapping mode AFM height and phase images of the sample in water (R = 1.28 nm; R_{max} = 11.3 nm)

Figure 4.2: AFM images of patterned PMMA surface in air and in water

4.1.1 Patterned polymethylmethacrylate (PMMA) surfaces

First set of nanopatterned surfaces used in this study consists of patterned polymethylmethacrylate (PMMA) surfaces. Figure 4.2(a) shows the schematic of the surface topology of the sample. The surface consists of regular patterns of pits in a PMMA matrix. The diameter of the pits is around 18 nm, whereas the depth of the pits is around 30 nm. The exposed surface at the base of the pits is hydrophilic silicon. Since we already know from the results in chapter 3 that PMMA is hydrophilic enough for nanobubbles not to occur, we can call this sample as "hydrophilic" nanopatterned surface.

Figure 4.2(b) shows the contact mode AFM height image of the sample in air. In this image, one can see patterns of pits (with pits diameter $\sim$ 18 nm) on a matrix. Though the patterns can be seen on the surface, the image is not very sharp in contrast. The roughness values for the image are R = 0.65 nm; $R_{\max}$ = 4.8 nm. This suggests that the vertical distance between the highest and the lowest points in the image is only around 5 nm, which is very less compared to the depth of pits ($\sim$ 30 nm). The reason behind low value of the observed depth size could be tip not being able to enter the pit completely. Figure 4.3 illustrates the above point. The schematic shows the situation when AFM probe is scanning over the patterned surface. The probe's end radius is around 15 nm which is around the size of diameter of the pits ($\sim$18nm).

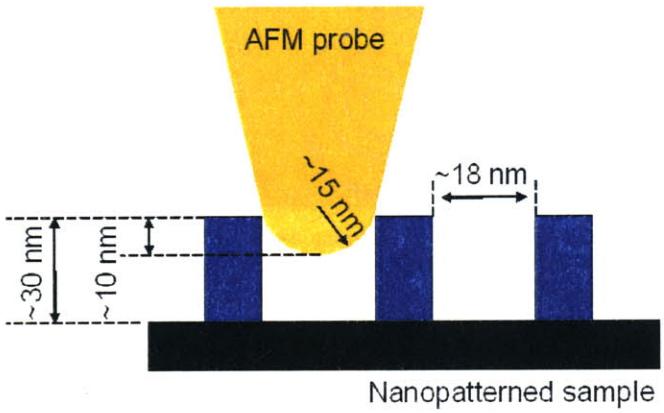

Figure 4.3: Schematic showing AFM probe not being able to penetrate the whole depth while scanning over a pit on nanopatterned surface

Figure 4.2(c) shows the tapping mode AFM height and phase images of the sample in water. The image looks similar to in-air image with regular patterns of pits. This time however,

the image has much better resolution compared to the in-air image. This may be due to better sensitivity of the instrument in tapping mode than contact mode. The roughness values are $R = 1.28$ nm; $R_{max} = 11.3$ nm. Besides the regular pattern of pits, there is no evidence of any other feature prbeesent on the surface. The roughness values for the image being close to the values for the in-air image supports this fact.

4.1.2 Patterned polystyrene (PS) surfaces

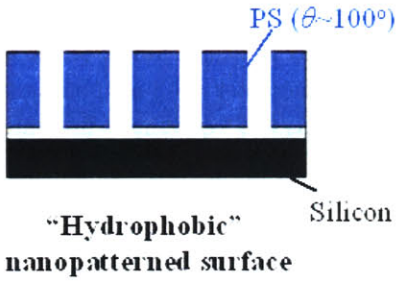

(a) Schematic of the sample

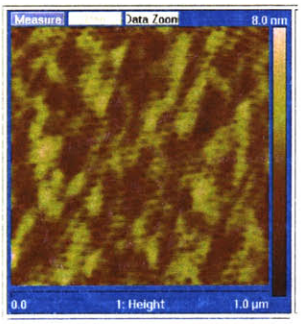

(b) Contact mode AFM height image of the sample in air ($R = 0.9$nm; $R_{max} = 8.2$ nm)

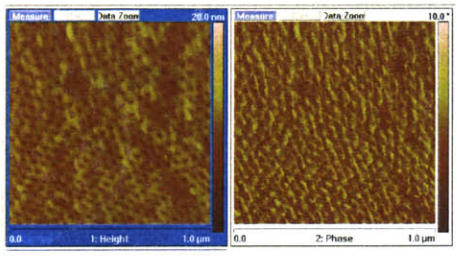

(c) Tapping mode AFM height and phase images of the sample in water($R = 1.12$nm; $R_{max} = 9.73$ nm)

Figure 4.4: AFM images of patterned polystyrene sample in-air and in-water

The second set of block-copolymer patterned surfaces presented here consists of patterned polystyrene (PS) surfaces. Figure 4.4(a) shows the schematic of the topology of the sample surface. The surface consists of regular patterns of pits in a PS matrix. The dimensions are similar to that of patterned PMMA surface. The diameter of the pits is around 20 nm where as the depth of the pits is around 30 nm. The exposed surface at the base of the pits is hydrophilic silicon. Since we have seen in chapter 3 that plain PS surface in water

is hydrophobic enough to support nanobubbles, we can call this surface as "hydrophobic" nanopatterned surface. Figure 4.4(b) shows the contact mode AFM height image of the sample surface in air. The image looks similar to that of patterned PMMA surface in air. The roughness values of the surface are $R = 0.9$ nm; $R_{max} = 8.2$ nm. R_{max} is again lower than the actual depth of pits for the same reason mentioned in previous section and shown in figure 4.3.

In chapter 3, we have seen that nanobubbles appear instantly on plain PS surfaces in water. This fact suggests that we can expect nanobubbles to appear on PS matrix in water. Figure 4.4(c) shows the tapping mode height and phase images of the sample in water. Contrary to our expectation, there appears to be no trace of nanobubbles anywhere in the images. The similar roughness values ($R = 1.12$ nm; $R_{max} = 9.73$ nm) to what was observed for the in-air image supports the fact that surface topology is same in air and in water for this case.

There are two possible arguments which can be given to explain this phenomenon of absence of nanobubbles on patterned polystyrene surfaces. First one originates from the lower value of macroscopic contact angle with water on this surface in comparison to the corresponding value for plain PS surface.

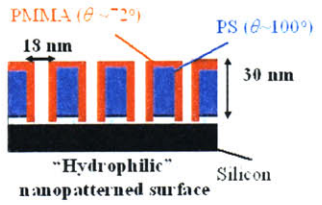

(a) Schematic of the "hydrophilic" sample

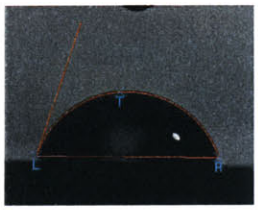

(b) $\theta = 69°$

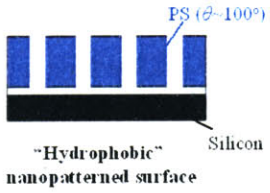

(c) Schematic of the "hydrophobic" sample

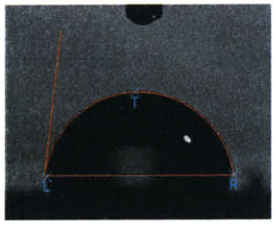

(d) $\theta = 81°$

Figure 4.5: Contact angle values with water on the nanopatterned surfaces

Figure 4.5 shows the respective macroscopic contact angles with water (θ) on the "hy-

Surface	f	θ_1	θ_2	$\theta_{\text{composite}}$
"hydrophilic"	0.85	72°	25°	69°
"hydrophobic"	0.7	100°	25°	81°

Table 4.1: Values for all the variables in Cassie-Baxter equation corresponding to patterned PMMA and patterned PS surfaces

drophilic" and "hydrophobic" patterned surfaces. Where as the the value of macroscopic contact angle of water on plain PS surface is $\sim$ 100°, the corresponding value for the "hydrophobic" patterned surface is only $\sim$ 81°. Similar observation is made for the "hydrophilic" patterned surface. The contact angle value is $\sim$ 69° in this case, which is less than the value on plain PMMA surface ($\sim$ 72°). The lower value of contact angle of water on the patterned PS surface suggests that the "hydrophobic" patterned surfaces may not be very hydrophobic at macroscale. This could explain the fact that nanobubbles don't appear on this sample.

Further, the macroscopic contact angle values on the above surfaces seem to be in accordance with Cassie-Baxter equation [15] for contact angle on composite surfaces. The equation 4.1 gives the contact angle value on composite surface as

$$\cos\theta_{AB} = f\cos\theta_A + (1-f)\cos\theta_B. \tag{4.1}$$

where θ_A is the contact angle value on plain surface of material A, θ_b is the contact angle value on plain surface of material B and f is the area fraction of material A in the composite. Filling in the values (given in table 4.1) for the two patterned surfaces, the Cassie-Baxter equation is found to be satisfied for both the surfaces.

The other argument in support of absence of nanobubbles on patterned PS surface originates from the fact that size of a typical nanobubble observed on plain PS surface is $\sim$ 150 nm which is much larger than the length of polystyrene material between any two pits on the patterned surface. This fact might suggest that the dimension of polystyrene between pits is too small to sustain nanobubbles.

4.2 Nanopatterned surfaces prepared using polymer spin-transfer printing

The second set of nanopatterned surfaces are fabricated using polymer spin-transfer printing technique and are provided to us by Prof. P. Hammond's research group at MIT. This set of nanopatterned surfaces consists of two different types of surfaces which are polystyrene dot patterned and OTS stripe patterned surfaces. Experimental results with these surfaces are presented in the subsequent sections.

4.2.1 Surfaces patterned with polystyrene posts

The first set of nanopatterned surfaces from Prof. Hammond's group discussed in this section consists of polystyrene dot patterned samples. Figure 4.6 shows the contact mode AFM height image of the sample in air. One can see the dot pattern in the image. However, the dot patterns do not seem to be very regular in their shape or size. This may be due to imperfect transfer of polymer at this location during printing which is not improbable.

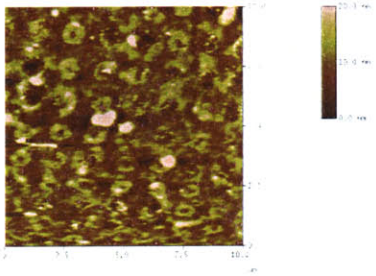

Figure 4.6: Contact mode AFM image of polystyrene dot patterned sample

Figure 4.7 shows the tapping mode AFM height and phase images of this sample in ethanol and in water. Where as the height images are not very different from each other, the phase images look different. One can see many small size round-shaped black spots over the PS dots in the phase image with water. This is not true for the image with ethanol. This distinct contrast in phase image for water which is not present for ethanol suggests the possibility of nanobubbles sitting on the PS dots. Further, the roughness values for height images of sample in-water ($R = 3.12$nm; $R_{\max} = 26.4$ nm) are higher as compared to values for the case of ethanol ($R = 2.89$nm; $R_{\max} = 17.5$ nm). Further evidences supporting the existence of nanobubbles on PS dots, besides dark spots disappearing upon harder tapping,

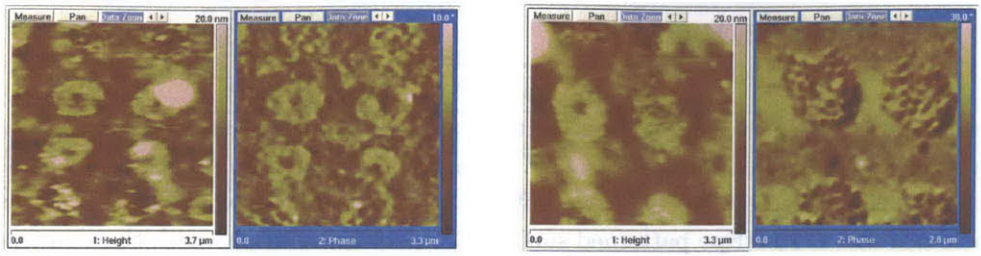

(a) in ethanol ($R = 2.89$nm; $R_{\max} = 17.5$ nm) (b) in water ($R = 3.12$nm; $R_{\max} = 26.4$ nm)

Figure 4.7: Tapping mode AFM height and phase images of PS dot patterned sample in ethanol and in water

include the size of these spots being of the same order as size of nanobubbles on plain PS surface.

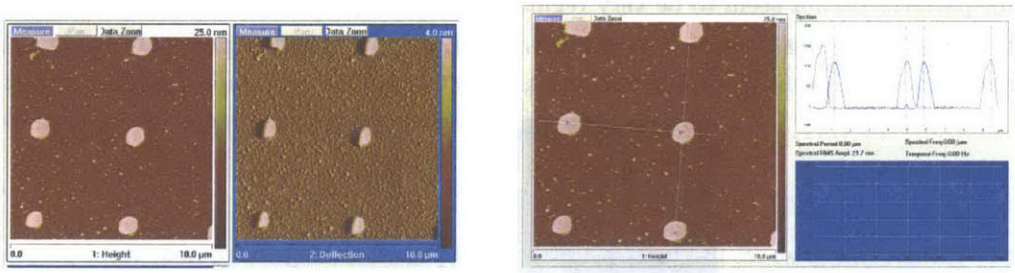

(a) Height and deflection (b) Section profile of the height image

Figure 4.8: Contact mode AFM images of the patterned PS dot surface with fiducial marks

As noted earlier, during patterning using the current method, polymer is not getting transferred equally well everywhere. There will always be some region with good pattern transfer consisting of distinct and regularly arranged dots and some region with imperfectly transferred patterns. Further, absence of control over the AFM probe location on the surface resulted in scanning of regions with imperfect pattern transfer which consequently led to bad images. To get around this problem, *fiducial* marks are used. The samples are first seen under a microscope, and the "good regions" are marked. The samples are then cut in such a way that the "good region" lies near the center of the sample. This made sure that the AFM probe (which usually sits over the center of the sample) scans this good region.

Figure 4.8(a) shows the in-air contact mode AFM images of the same sample, this time with fiducial marks. The image looks more clear as compared to previous ones. Figure 4.8(b)

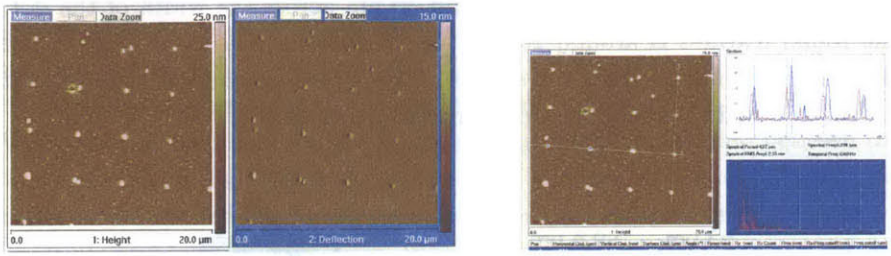

(a) Height and deflection (b) Section profile of height image

Figure 4.9: In-air contact mode AFM images at second location on patterned PS dot surface with fiducial marks

shows the section profile across these spots. Whereas the diameter and height of the dots (posts) are around 1μm and 100 nm respectively, the pitch in both x- and y- direction is $\sim 4.7\mu$m.

One thing to notice here is that although the patterns are uniformly spaced, there still remains variation in height of the posts. Figure 4.9 shows the dot pattern at a different locations in the "good region". One can see from the section image in figure 4.9(b)that the diameter and height of these posts are around 0.6μm and 12 nm respectively. These values are much lower as compared to height and diameter of dot patterns in figure 4.8(b). The pitch in both x- and y- directions is however the same ($\sim 4.7\mu$m).

It is important to note here that the difference in height values of the PS dots at different locations would make it difficult to calculate the height of nanobubbles in in-water images. Further, the roughness values for the background are $R \sim 1$ nm and $R_{\max} \sim 10$ nm.

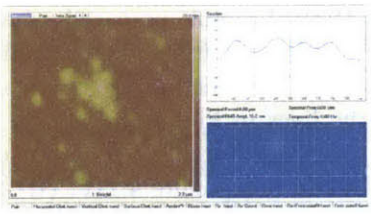

Figure 4.10: Section image of PS posts showing nanobubbles in TM-AFM water

Figure 4.10 shows the in-water tapping mode AFM image of the sample along with a height profile along a section on a single dot. One can see small round-shaped features sitting over the dot while the background surface is almost featureless. Further, the height profile in

the section window is oscillating between 10 and 20 nm across the width of the dot. The width of the round features is around 200nm. All these numbers are similar to numbers corresponding nanobubbles on plain PS surface. The above mentioned facts suggest that PS dots present in a hydrophilic matrix can support nanobubbles.

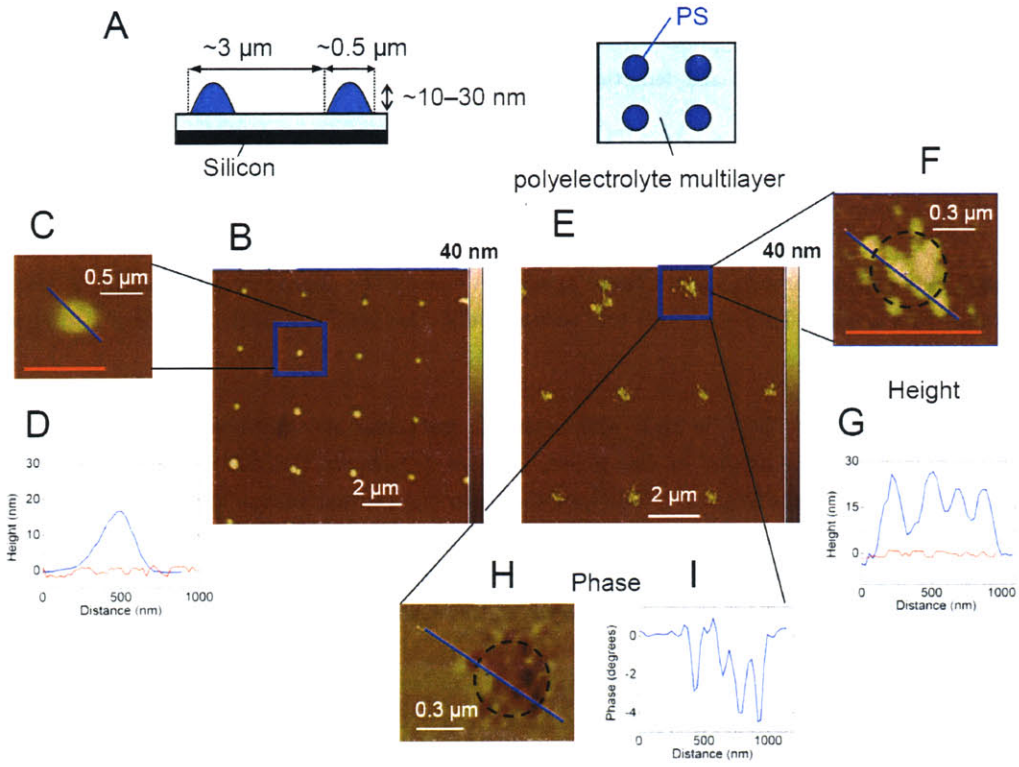

Figure 4.11: Results with nanopatterned sample prepared using polymer transfer printing. (A) a schematic diagram of the topology of the surface (not to scale), (B) contact-mode AFM height image of sample in air, (C) zoomed image of one of the dots in Figure 4.11B. (D) cross-sectional views along the lines in Figure 4.11C, (E) tapping-mode AFM height image with sample in water. (F) zoomed height image of one of the dots in Figure 4.11E, (G) cross-sectional views along the lines in Figure 4.11F, (H) zoomed phase image of one of the dots in Figure 4.11E, (I) cross-sectional view along the line drawn in Figure 4.11H

Figure 4.11 shows further images obtained in tapping mode AFM scanning of the sample in water. Figure 4.11A shows a schematic diagram of the surface topology, which consists of a regular pattern of PS dots (pitch $\sim 3\mu$m) in a hydrophilic polyelectrolyte multilayer [poly-(diallyldimethyl ammonium chloride) (PDAC)/poly (styrene-4-sulphonate)]5.5 matrix. The height and diameter of the dots are $\sim 10-30$ nm and ~500 nm, respectively. Figure 4.11B

shows the contact-mode AFM height image of the sample in air. We see regularly arranged dot structures with diameter ~500 nm and height $\sim 10-30$ nm in a featureless background with roughness values of R = 0.36 nm and R_{max}= 1.8 nm (Figure 4.11B, C and D). Figure 4.11E shows the tapping-mode AFM height image when the same sample is immersed in water. While there is no difference in the topography of the background between the height images in Figure 4.11B and Figure 4.11E, we see a significant difference in topography at the locations of the PS dots in the two images. When the sample is immersed in water, we observe multiple circular-shaped features appearing together in the height and phase images only at the PS dots (Figure 4.11E, F and H). The height profile across a dot (Figure 4.11F), unlike that in Figure 4.11D, shows multiple individual peaks corresponding to protuberances in the shapes of spherical caps rather than a single peak corresponding to the dot. The height and width of these individual protuberances, after removal of the contribution from the PS dots,are $\sim 5-15$ nm and $\sim 100-200$ nm, respectively. These values are similar to the dimensions of nanobubbles observed on homogenous PS surfaces. The significant change in the phase of these features that is observed at each of the PS dots is consistent with our earlier results, in which a similar phase variation for nanobubbles on homogenous PS surfaces was found. Further, we observed a significant effect of tapping force on the morphology of these features during scanning. Upon harder tapping the features shown in Figure 4.11are $\sim 5-15$ nm and $\sim 100-200$ nm, respectively. These values are similar to the dimensions of nanobubbles observed on homogenous PS surfaces. The significant change in the phase of these features that is observed at each of the PS dots is consistent with our earlier results, in which a similar phase variation for nanobubbles on homogenous PS surfaces was found. Further, we observed a significant effect of tapping force on the morphology of these features during scanning. Upon harder tapping the features shown in Figure 4.11F and H disappeared. Thus, we can conclude that the observed features that develop on the PS dots are nanobubbles with dimensions similar to the nanobubbles observed on flat PS surfaces. The results are mentioned in detail elsewhere [3].

4.2.2 Surfaces patterned with stripes of octadecyltrichlorosilane (OTS)

Last set of patterned surfaces discussed in this chapter consists of octadecyltrichlorosilane (OTS) stripe patterns. The spacing between two consecutive stripes is ~ 200 nm. Method of preparation of this surface is given in more detail in chapter 2. Figure 4.12 shows the tapping mode AFM height and phase images of this surface in water. One can see round features in both height as well as phase images distributed on mostly the striped regions. Corresponding to locations of these features in the height image, there is a sharp change in phase which is indicative of the distinct change in properties at these locations. Further, the shape (round, discrete) and dimensions of these features are similar to nanobubbles on a OTS hydrophobized surface. All these facts suggest that the features are nanobubbles

and that the stripe patterns are good enough to support the nanobubbles.

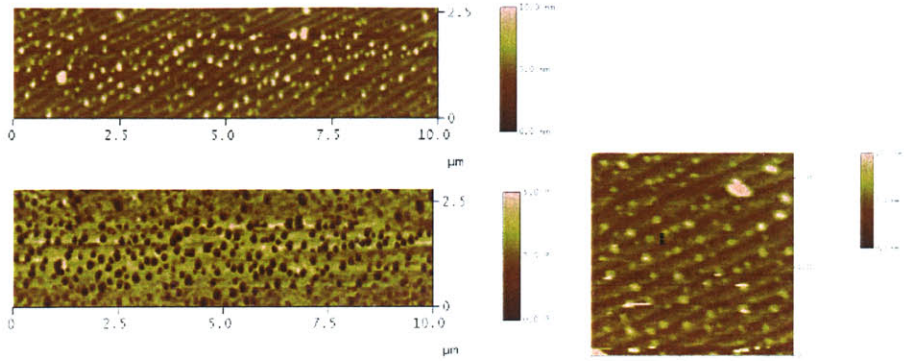

(a) Height and Phase image

(b) Zoomed image

Figure 4.12: Tapping mode images of the nanobubbles on stripe pattern of OTS on silicon

Chapter 5

Quantitative analysis

MOST of the papers on nanobubbles available in literature - which itself are few in number - give qualitative discussion on nanobubbles. Very few of these papers give quantitative information about different bubble parameters. These bubble parameters could include bubble height, radius of curvature, area and volume coverage (both of individual bubble and of all the bubbles present in the scanned image), number of nanobubbles in unit area, pressure inside the bubble etc. One of the aims in this study is to establish the trends in these different bubble parameters with surface hydrophobicities and gas solubilities in different solvents. Before presenting the trends in these parameters with different experimental conditions, a discussion on certain post-processing tools used to get the correct bubble parameters is discussed first in the subsequent sections.

5.1 Calculation of morphological parameters for nanobubbles

From the experiments it is found that shapes and sizes of bubbles vary significantly from one bubble to another. Even bubbles from one image show significant variation in shapes and sizes among themselves as shown in figure 5.1.

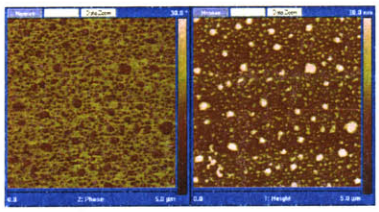

Figure 5.1: Variation in shapes and sizes of nanobubbles in an AFM image (from tapping-mode AFM imaging on OTS hydrophobized silicon)

The above observation suggests that a statistical method of analysis based on a large sample

set is required for any quantitative deduction to be meaningful. Based on this fact, for a given type of surface, number of different samples are used for experiments. Best images corresponding to each sample is taken for detailed image analysis. Equal number of bubbles are selected for analysis from each image to avoid any bias for any image. The sample set for each surface then consists of $\sim$ 100 data points, corresponding to that many nanobubbles.

Figure 5.2(a) shows the section profile across a single nanobubble sitting on polystyrene surface. The image is obtained by tapping mode AFM imaging of polystyrene in water. The profile looks like smooth symmetric lobes. This observation was found to be true for almost all the bubbles.

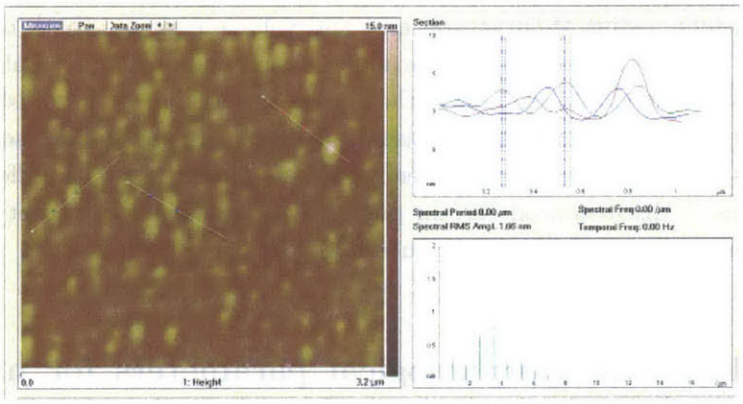

(a) Section across nanobubbles(from tapping mode AFM height image of polystyrene in water)

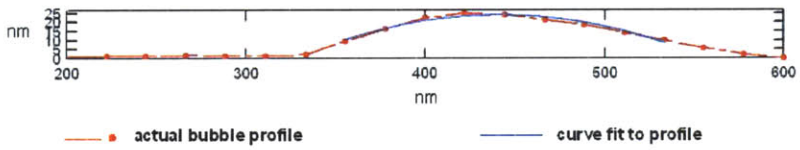

(b) Cross-section profile of bubble plotted along with the fitted spherical cap in 1:1 scale

Figure 5.2: Curve fitting of actual bubble profile

Exporting the section profile into IGOR Pro software and carrying out curve-fitting to this profile, shows that the bubble profile fits very well with a spherical cap profile(figure 5.2(b)). The red curve is the actual bubble profile where as the blue profile is the fitted spherical cap. The figure shows that bubbles are not complete spheres in themselves but are just the spherical caps with high aspect ratios.

Figure 5.3 shows a schematic diagram of the bubble profile drawn as spherical cap from

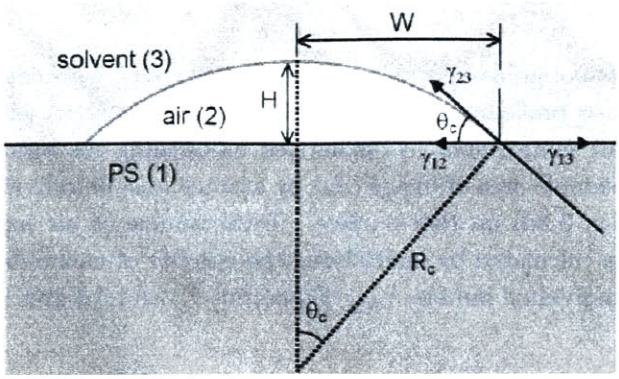

Figure 5.3: Schematic of bubble cap used for calculation of bubble parameters

which different bubble parameters can be calculated. The bubble height at its center (H) and the half-width (W) can be directly measured from the cross-section profile. Equations 5.1 can be used to calculate few more parameters.

$$\theta_c = 2\tan^{-1}\left[\frac{H}{W}\right] \tag{5.1a}$$

$$R_c = \left[\frac{W^2 + H^2}{2H}\right] \tag{5.1b}$$

$$P_{in} = P_{out} + \left[\frac{2\gamma_{lv}}{R_c}\right] \tag{5.1c}$$

In the above equations, θ_c is the air-side contact angle of bubble, R_c is the radius of curvature of the bubble, P_{in} is the pressure inside the bubble, P_{out} is the pressure in the solution, and γ_{lv} is the surface tension of the bubble-liquid interface.

From the parameters calculated from section profile and equations 5.1, few more parameters viz. area of bubble-sample contact region per bubble (A_b) and volume of gas inside a bubble (V_b) can also be calculated using equations 5.2.

$$A_b = \pi W^2 \tag{5.2a}$$

$$V_b = \frac{\pi}{6}\left[3W^2H + H^3\right] \tag{5.2b}$$

Total area covered by nanobubbles per unit sample surface area (A_t) is determined by using a rigorous image analysis procedure described later in this chapter. A normalized number of nanobubbles per unit sample area ($\bar{N}$) is derived by dividing the total area covered by nanobubbles per unit sample area of image (A_t) by average area of individual bubble, A_{avg} (calculated by Equation 5.3a) on that surface. Total volume of air inside nanobubbles per unit sample area is calculated by multiplying the number of nanobubbles ($\bar{N}$) and the average volume of an individual bubble, V_{avg}. Equations 5.4 and 5.3 give the mathematical relations.

$$A_{avg} = \frac{\sum_{i=1}^{100} A_b}{100} \tag{5.3a}$$

$$V_{avg} = \frac{\sum_{i=1}^{100} V_b}{100} \tag{5.3b}$$

$$\bar{N} = \left[\frac{A_t}{A_{avg}}\right] \tag{5.4a}$$

$$V_t = \bar{N}\, V_b \tag{5.4b}$$

Finally, to complete the above set of equations we need to find the area covered by nanobubbles per unit sample area (A_t). This is obtained through an area analysis algorithm described in next section. Contact angle (θ) with water is used as a measure of hydrophobicity of sample.

5.2 Area analysis

A rigorous area analysis procedure is used to calculate the correct area of nanobubbles in a given image.

AFM software, Nanoscope version 5.12 has a *particle analysis* module which can be used to calculate area percentage. Figure 5.4 shows how this module works.

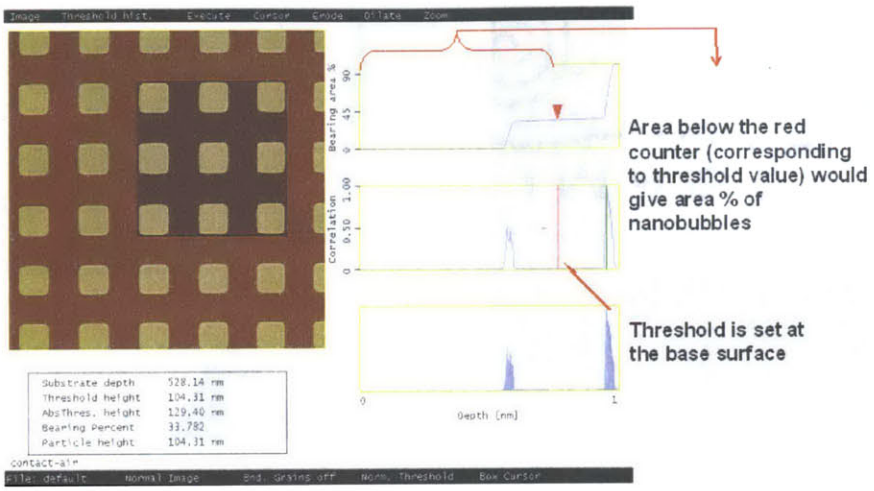

Figure 5.4: Area analysis of calibration sample image using *particle analysis* module available in Nanoscope version 5.12 software

The AFM image in figure 5.4 is of calibration sample imaged in contact mode in air. The three boxes to the right of the image in the figure are *bearing ratio curve,correlation histogram, depth histogram* from top to bottom respectively. The correlation histogram shows number of pixels corresponding to pixel height. One can set the threshold manually at any pixel height by sliding the red bar in the correlation histogram. Once the threshold is specified, the software calculates the total number of pixels which are above the threshold. The ratio of the total number of pixels with height above the threshold value to total number of pixels in the image is given as a percentage, which is called *bearing percent*. This value can be read from the box under the image in the figure 5.4.

In figure 5.4, we can see that there are two peaks in the histogram, one corresponding to height of substrate and the other corresponding to height of pits. In this case, it is easy to set the substrate threshold. Since there are hardly any pixels in between the two peaks, setting the threshold anywhere between the two peaks would give approximately the same answer. In figure 5.4 bearing percentage is calculated to be ≈ 33.3, which is very close to the value of theoretical area percentage of the pits in the shaded square region.

Though the above procedure works well for area analysis of calibration sample, it is not very robust for the images containing nanobubbles. To understand this, let us take a look

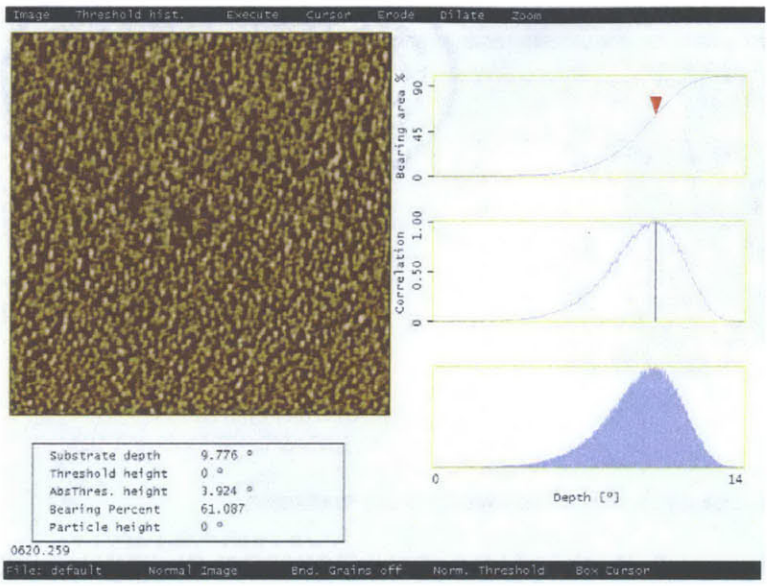

Figure 5.5: Area analysis of an AFM image containing nanobubbles on a polystyrene surface using *particle analysis*

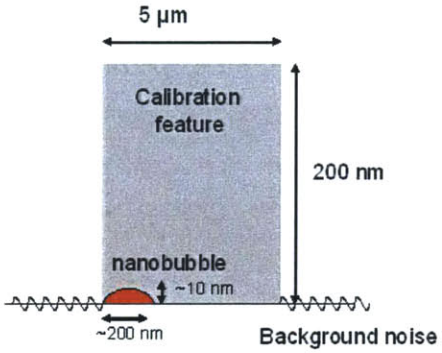

Figure 5.6: Schematic showing the relative surface height for background, feature on the calibration sample, and a typical nanobubble (x- and y- scales are different)

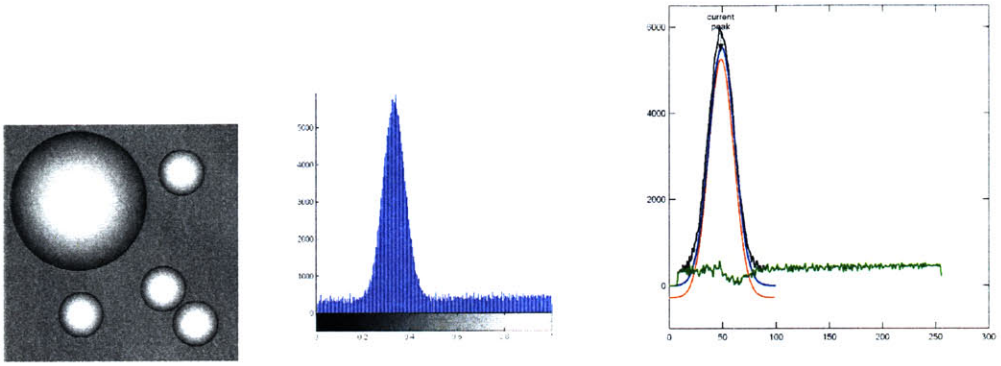

(a) Model surface generated in MATLAB

(b) Histogram of the image

(c) IGOR Pro peak-fit analysis of histogram image to eliminate the peak corresponding to gaussian noise

Figure 5.7: Area analysis on an artificially generated model surface using MATLAB

at figure 5.5. This time the correlation histogram does not show two distinct peaks as it did in previous case with calibration sample. The fact that there is only peak in the histogram, makes it more difficult to set the threshold. The reason behind only one peak in the correlation histogram might be the size of nanobubbles being small enough to be around the order of the noise in background. This idea is illustrated in figure 5.6.

To get around this problem, a MATLAB algorithm is developed to compute the correct area percentage of nanobubbles in a given image. Figure 5.7 shows the procedure on an artificially generated model surface with known area% of spherical caps. Figure 5.7(a) shows the model surface with spherical caps of different sizes in a background filled with gaussian distributed noise. Maximum height of the cap is set at 60 nm. The mean of gaussian distribution in noise is set as 10 nm where as the standard deviation is set as 2.8 nm. Theoretical value of the area% of spherical caps is 38.9.

Histogram of the above image is calculated and is shown in figure 5.7(b). The histogram shows that a portion of the area corresponding to the spherical caps (straight line in the graph) is buried under the peak corresponding to gaussian noise in the background. To calculate the correct area% corresponding to the spherical caps, the gaussian peak needs to be separated from the rest of the data.

Removal of noise from the histogram is done with the help of peakfit analysis module available in IGOR Pro software. The histogram profile is exported from MATLAB to IGOR Pro. Peakfit analysis separates the original profile into two daughter profiles. One of the

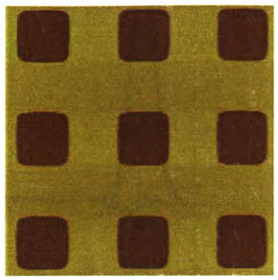

(a) AFM height image of the calibration sample

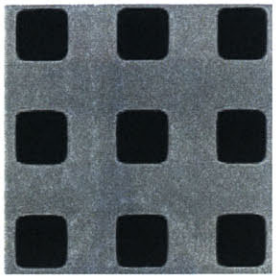

(b) Intensity image generated from the AFM image

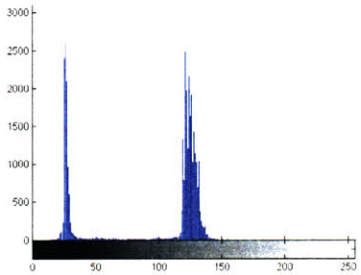

(c) Histogram of the image

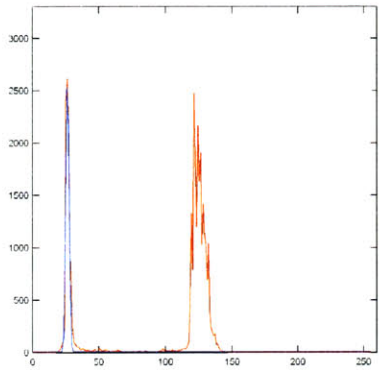

(d) Area under the curve calculation in IGOR Pro

Figure 5.8: Area analysis of the AFM image of calibration sample using MATLAB and IGOR Pro peak fit analysis

profile fits the peak and corresponds to the gaussian noise where as the other profile is the residual curve and corresponds to the spherical caps in this case. Figure 5.7(c) shows the histogram after a peak-fit analysis. Calculating the area under the residual curve gives the area percentage to be 38 which is close to the theoretical value (38.9).

Figure 5.8 shows the above analysis for the calibration sample image. It can be seen here that the histogram image contains two distinct regions, one corresponding to the background and one corresponding to the features. The area under the peak corresponding to features, is found to be 36.3 % which is close to the theoretical value of 36%.

Figure 5.9 shows the above analysis for an actual AFM image containing nanobubbles.

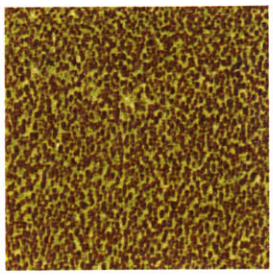

(a) AFM phase image showing nanobubbles

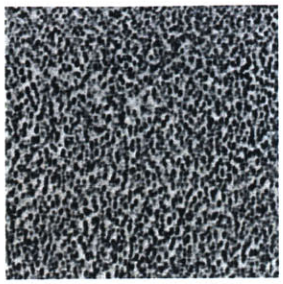

(b) Intensity image generated from the AFM image

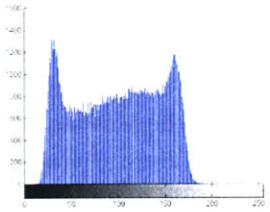

(c) Histogram of the image

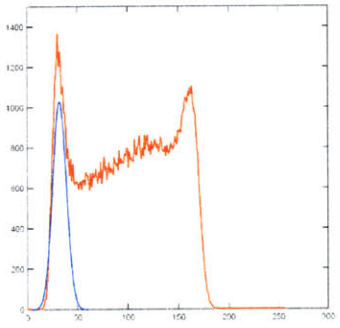

(d) IgorPRO peak-fit analysis

Figure 5.9: Area analysis of an AFM image containing nanobubbles using MATLAB and IGOR Pro peak fit analysis

It is also worth mentioning that for area analysis, phase images are better suited as compared to height image because phase images have better color contrast.

5.3 Trends in bubble parameters with surface hydrophobicity

Making use of equations 5.1-5.4, and area analysis algorithm, we can get all the relevant bubble parameters mentioned earlier in the chapter. For each of the variables corresponding to a surface, all the values are found to follow a normal distribution. Hence hereafter,

the values of different bubble parameters would be reported in mean and standard deviation. Table 5.1 lists the values of different bubble parameters for some of the homogenous hydrophobic surfaces used in the study.

The values of each parameter can also be plotted with respect to surface hydrophobicity (measured in terms of contact angle with water) to observe the trends in different bubble parameters with hydrophobicity (Figures 5.10 and 5.11).

The width of the bubbles tend to become larger with increasing hydrophobicity. This also results in the average area per nanobubble, A_{avg}, increasing with hydrophobicity. A_{avg} is calculated using 5.3a.

From area analysis the total area per unit image area is found to be decreasing with increasing hydrophobicity. Since total area is decreasing and average area per bubble is increasing, this directly gives us that the number of nanobubbles is decreasing with increase in hydrophobicity. This can also be seen visually as bubbles become less frequent on more hydrophobic samples. The height of the bubble is also increasing with increase in hydrophobicity. The average volume of individual bubble,V_{avg} (Equation 5.3b) is getting larger with hydrophobicity since both height as well as width is increasing with hydrophobicity. The radius of curvature which has a strong dependence on the height of the bubble along with width of bubble increases rapidly with increase in hydrophobicity. The internal pressure which is inversely proportional to the radius of curvature decreases sharply with increase in hydrophobicity.

Sample	Average height (H) nm	Average width (W) nm	Radius(R_c) nm	Contact angle (θ_c) degrees	Pressure (P_{in}) atm
PS	6.0 ± 2.5	$0.8 \times 10^2 \pm 20$	$5.3 \times 10^2 \pm 1.8 \times 10^2$	7.4 ± 2.8	3.5 ± 0.9
Si+OTS	13 ± 4.2	$1.2 \times 10^2 \pm 31$	$6.1 \times 10^2 \pm 2.3 \times 10^2$	13 ± 3.8	3.1 ± 0.7
rGlass+OTS	17 ± 4.8	$1.7 \times 10^2 \pm 36$	$7.2 \times 10^2 \pm 2.8 \times 10^2$	15 ± 3.2	2.8 ± 0.8

Table 5.1: Different bubble parameters on homogenous surfaces

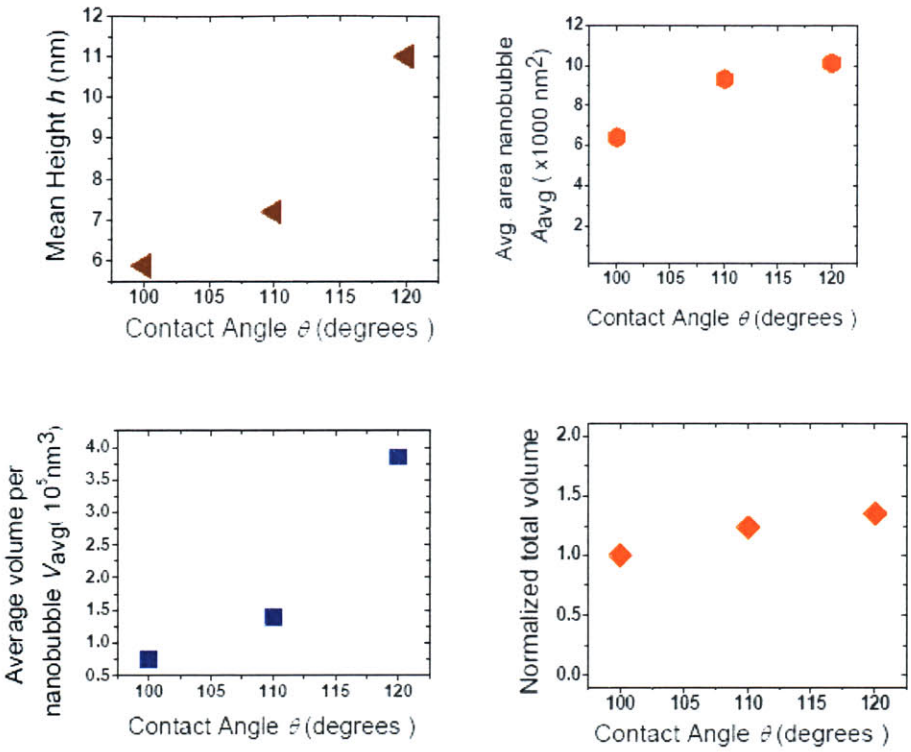

Figure 5.10: Variation in bubble height, average base area of a nanobubble, average bubble volume and total volume with surface hydrophobicity

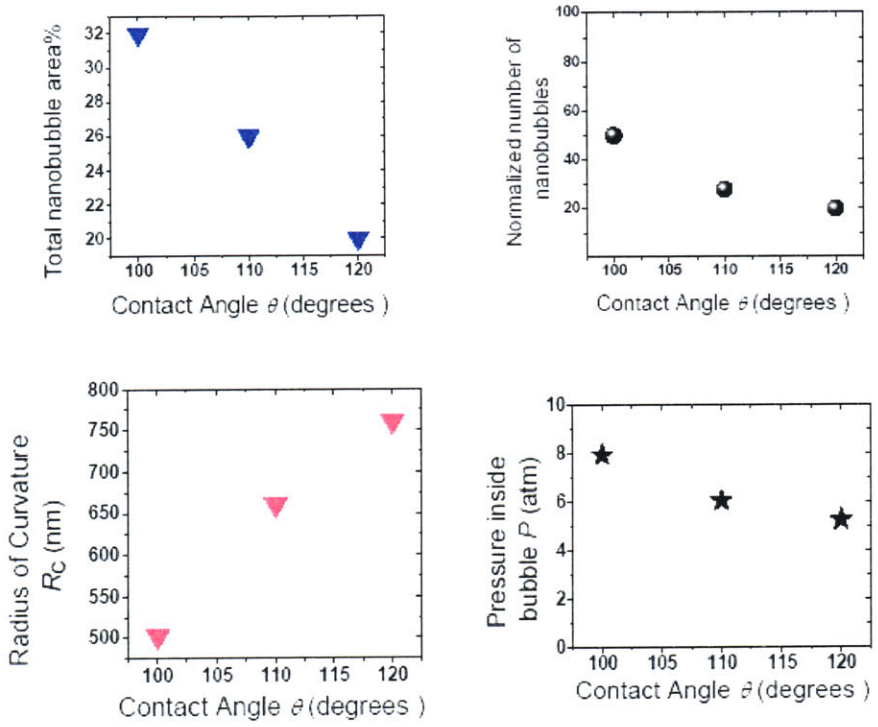

Figure 5.11: Variation in radius of curvature, mean pressure inside the nanobubble, total area coverage and total number of nanobubbles with surface hydrophobicity

5.4 Effect of line tension

The influence of line tension has been proposed elsewhere [61] as a force which might stabilize the nanobubbles and reduce the Laplace pressure inside them. When the size of a droplet or bubble is small, effect of line tension shows up in the Young's equation.

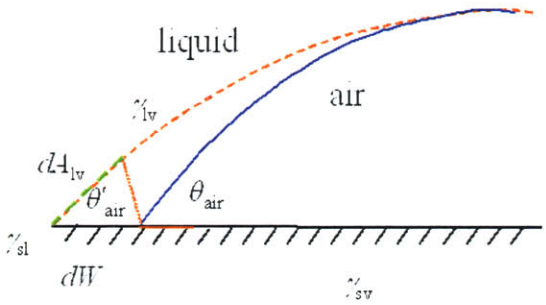

Figure 5.12: Changes in respective surface areas contact lines upon deformation in bubble from its equilibrium state

Let us go back and write the Gibbs free energy change associated with deforming the bubble at its equilibrium state by an infinitesimal amount. Based on figure 5.12, we can write the relations as given in equations 5.5.

$$dG = (\gamma_{sv} - \gamma_{sl})\, dA_{sl} + \gamma_{lv} dA_{lv} + \tau dl \tag{5.5a}$$

$$dA_{sl} = 2\pi W dW \quad dl = 2\pi dW \quad dA_{lv} = 2\pi W \cos(\theta_c) dW \tag{5.5b}$$

$$\gamma_{lv} \cos(\theta_{air}) = (\gamma_{sl} - \gamma_{sv}) - \frac{\tau}{W} \tag{5.5c}$$

$\theta_{air}$is the actual microscopic contact angle, τ is the line tension. The equation 5.5c suggests that a linear relation can be expected between $\cos(\theta_{air})$ and $1/W$ (inverse half-width). The equation 5.5c also gives the relation (equation 5.6) used to calculate the length-scale at which line tension effects become important.

Carrying out a simple order-of-magnitude calculation (equation 5.6), one can see that line tension effects become important at length-scales $\sim$ 1 nm.

$$l \approx \frac{\gamma}{\tau} = \frac{10^{-10}\ \text{N}}{72\ \text{mN/m}} \sim 1\ \text{nm} \tag{5.6}$$

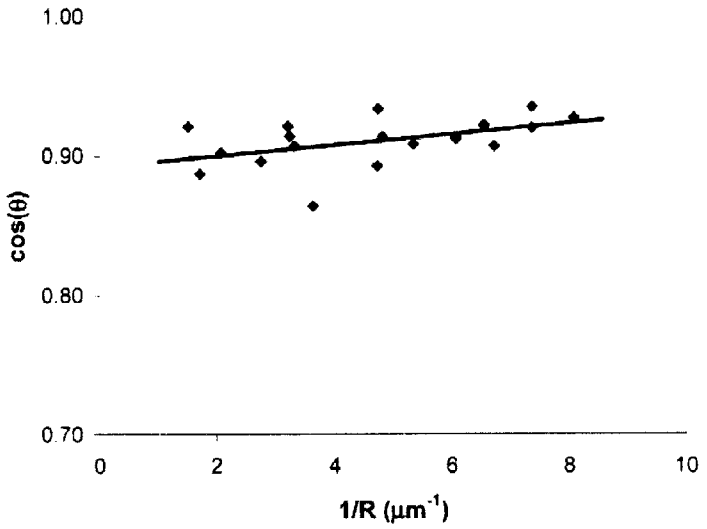

Figure 5.13: Scaling of air-side contact angle of nanobubbles with inverse of radius of curvature (from Yang *et* al. [61])

To show the importance of line tension in the context of nanobubbles, Yang *et* al. [61] have plotted $\cos(\theta_{air})$ against inverse of radius of curvature $(1/W)$, where θ_{air} is the air-side contact angle of the bubble. The plot is shown in figure 5.13. Further, they relate the positive slope in the graph to $-\tau/\gamma$ to calculate the value of τ as -3×10^{-10} N.

Figure 5.14 shows the dependence of the microscopic air-side contact angle on the corresponding inverse of radius of curvature of the three-phase contact line for nanobubbles observed on PS and silanized silicon surfaces. The data look similar to those of Yang *et* al. [61]. Fitting a straight line profile to the data, we get straight line fits with positive slope for both types of surfaces. The values of line tension calculated from the gradient of the regression line are -1.6×10^{-12} N for PS and -3×10^{-11} N for silanized silicon samples. These values are comparable to -3×10^{-10} N obtained by Yang *et* al. [61]. However, if we see the inset of Figure reffig:mylinetensiontrend, in which the ordinate axis is rescaled and zoomed in, we find that the data look very scattered. We observe that the cosine of the microscopic air-side contact angle varies in a very small range (0.01) close to its up-

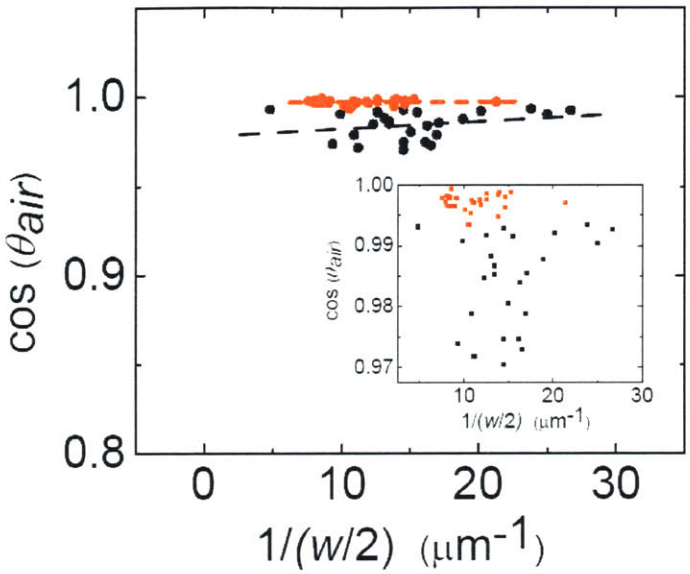

Figure 5.14: Scaling of air-side contact angle of nanobubble with inverse of half-width for data in the study

per limit value of 1. In conclusion, the results in this study suggest that the microscopic contact angle is independent of any effects of curvature or line tension forces. A simple order-of-magnitude estimate (Eq. 5.6) gives the relevant length-scale at which the effect of line tension become significant as ~1 nm.

The relevant length scale in the present problem which is the half-width of nanobubbles has a value of the order of 100 nm. This value is two orders of magnitudes higher than the magnitude of the relevant length scale for line tension effects to become significantly important. The size of the bubbles in Yang *et* al. [61] is still higher ($\sim$ 500 – 800 nm) and thus one would imagine the line tension effects to be negligible for the nanobubbles observed in their experiments.

5.5 Estimation of interfacial slip

An analytical model has been developed elsewhere [56] to quantify the effects of partial nanobubble coverage on pressure-driven fluid flow between two infinite parallel plates. The following equation for the slip length (β) is obtained as a function of plate separation (D), air gap thickness/bubble height (h), and area fraction (ϕ)of nanobubbles.

$$\beta = \frac{2\phi\mu_w}{\mu_a(2-\phi)D}\left(\frac{2}{3}\lambda h + \frac{h^2}{2} + \left(\frac{2}{3}\lambda + h\right)D\right) \tag{5.7}$$

Here μ_w, μ_a are the viscosities of water and air at 20°C respectively, and λ is the mean free path of the gas inside the bubbles. Plugging in the respective values for different variables as follows, ϕ= 0.32, μ_w = 1.0019 cp, μ_a = 0.0183 cp, D = 10 μm, h = 13 nm, λ = 100 nm, we calculate the slip length (β) to be $\sim 1 - 2\mu m$ for water flowing over the hydrophobic surface. The consistency of the calculated slip length with experimental values reported in the literature, suggests that the apparent fluid slip observed experimentally at hydrophobic surfaces may indeed arise from the presence of nanobubbles.

Chapter 6

Thermodynamic issues with nanobubbles

6.1 Stability of nanobubbles

ONE of the major issues that must be faced in believing the existence of nanobubbles is the origin and stability of the nanobubbles. The problem revolves around the Young-Laplace equation given as follows:

$$P_{in} = P_{out} + \left[\frac{2\gamma_{lv}}{R_c}\right] \tag{6.1}$$

The above equation shows that the pressure inside the nanobubble (P_{in}) is greater than pressure in the solution (P_{out}) by an amount proportional to the surface tension of the liquid-vapor interface (γ_{lv}), and inversely proportional to the radius of curvature of the nanobubble (R_c).

In some of the early papers on nanobubbles in literature, half-width of the bubble (W) is mistakenly used in the above equation instead of the radius of curvature, because of which, a very high value of internal pressure ($\sim$ 100 atm) was obtained for a typical nanobubble [7, 28]. The fact that nanobubbles appear to be in equilibrium and do not collapse even with pressure inside being very high, baffles the researchers. However, as noted in a recent paper [47] and also in chapter 5 of this thesis, the actual radius of curvature is found out to be much larger than the half-width of nanobubbles. The higher value of radius of curvature leads to a relatively lower value of pressure. As calculated in chapter 5, the pressure inside the nanobubbles on polystyrene surface is $\sim 4.2 \pm 1.7$ atm. The above value of pressure being of the order of 1 atm is consistent with stability of nanobubbles although the value being higher than atmospheric pressure requires further explanation.

6.2 Debate over existence and equilibrium of nanobubbles

While the experimental evidence, as reviewed elsewhere [8], shows that nanobubbles exist and are the origin of the measured long-ranged hydrophobic attractions, the theoretical understanding of the nanobubble phenomenon is not so advanced. There remain unanswered a number of questions regarding their shapes, origin and stability. There is an apparent paradox between the observed occurrence and stability of nanobubbles and the Laplace-Young equation (Equation 6.1).

Equation 6.1 gives an excess pressure of 5–30 at. for the observed range of sizes of nanobubbles in the literature. With such a high internal pressure, nanobubbles can not be in equilibrium with the atmosphere and should dissolve rapidly in the solution [8]. Thus, the fact that nanobubbles appear to be in equilibrium and do not collapse during AFM scanning has yet to find a theoretical explanation. Different hypotheses have been proposed in the literature in an attempt to reconcile the observed occurrence and stability of nanobubbles with a full theoretical understanding. Line tension along the base of nanobubbles has been suggested as the force keeping the bubble stable and explaining the high apparent pressure within the bubble [61]. Another possible hypothesis conjectures that the nanobubble may not be in equilibrium with the solution, or if they are in equilibrium, they are so with a supersaturated solution [8]. The applicability of the unmodified Laplace-Young equation (Eq. 6.1) to nanobubbles for calculating the internal pressure has also been questioned [8]. Further, while some studies show that the nanobubble may be stabilized by long-range attraction forces [57, 58], others suggest that nanobubbles can be formed that are not stabilized by long-range interactions [47]. The shapes and sizes of the observed nanobubbles in the literature show strong variability as well. Nanobubbles are observed to be both as distinctly non circular in shape with a high area coverage [57], and as hemispherical objects of uniform circular cross section spatially separated from each other [61, 27]. Solvent polarity has also been found to have an influence on the morphology of nanobubbles [47].

6.3 Inapplicability of classical Young-Laplace equation

Since we already know the volume, pressure and temperature inside a typical nanobubble (calculated in chapter 5), we can easily make an estimate of number of gas molecules inside a nanobubble. Assuming that the gas inside is only air and that the gas behaves as an ideal gas, we can use the ideal gas law (equation 6.2) to calculate the number of molecules present inside a nanobubble. In reality, there will be little amount of water vapor present in the nanobubble as well. For the first order approximation, the contribution from water vapor can be neglected as the mole fraction of water vapor would be much less compared

to that of air inside the nanobubble.

$$P_{in} V_b = nRT \tag{6.2}$$

In the above equation, R is the universal gas constant (0.082 l atm K $^{-1}$ mol^{-1}), T is temperature (K), n is the number of moles of gas (mol). Plugging in the values for known quantities (P_{in} = 5 at., $V_b = 1.6 \times 10^5\,\text{nm}^3$, T = 298 K), gives number of molecules as $\sim$ 20,000. The number is not very high as compared to number of molecules in a typical macroscopic problem ($\sim 10^{23}$).

Further, mean free path (λ) of air molecules—the distance travelled by a molecule before it collides with another—inside the bubble can be calculated using the Equation 6.3.

$$\lambda = \frac{1}{\sqrt{2}\pi d^2 n} \tag{6.3}$$

d is the diameter of an air molecule and n is the number of molecules per unit volume. Plugging in the respective values, gives the mean free path value to be around 20–30 nm.

Thus, the mean free path comes out to be around the same size as height of the bubbles in this case. In practice, theory suggests that the area need only be larger than about 10 times the square of mean free path, so that pressure is a continuum property. In other words, for areas of engineering interest, which are almost always much larger than areas measured in terms of the mean free path, the pressure does not have any measurable statistical fluctuations caused by molecular motions. We can then make a distinction between microscopic properties and the macroscopic properties of a fluid, where the microscopic properties relate to the behavior on a molecular scale (that is, scales comparable to the mean free path), and the macroscopic properties pertain to the behavior on an engineering scale (that is, scales much larger than the mean free path).

The above observation suggests that the macroscopic pressure definition is not applicable at the given length scale of this problem, and thus it puts a question mark on the validity of Young-Laplace equation for very small length-scale problems.

6.4 Effect of long range forces in stabilizing the nanobubbles

While for most part, the shapes of the nanobubbles are well approximated by spherical caps with width much larger than the height; in the vicinity of the three phase contact line, the shapes deviate from the spherical cap profile to merge with the solid surface at a slope of nearly equal to zero. This deviation in the interfacial profile from the spherical cap shape could be due to long-range van der Waals forces, which are relevant at a spatial scale of few nanometers from the solid surface.

A discussion of such profiles when the contact angle θ_e becomes small is given in detail elsewhere [21].

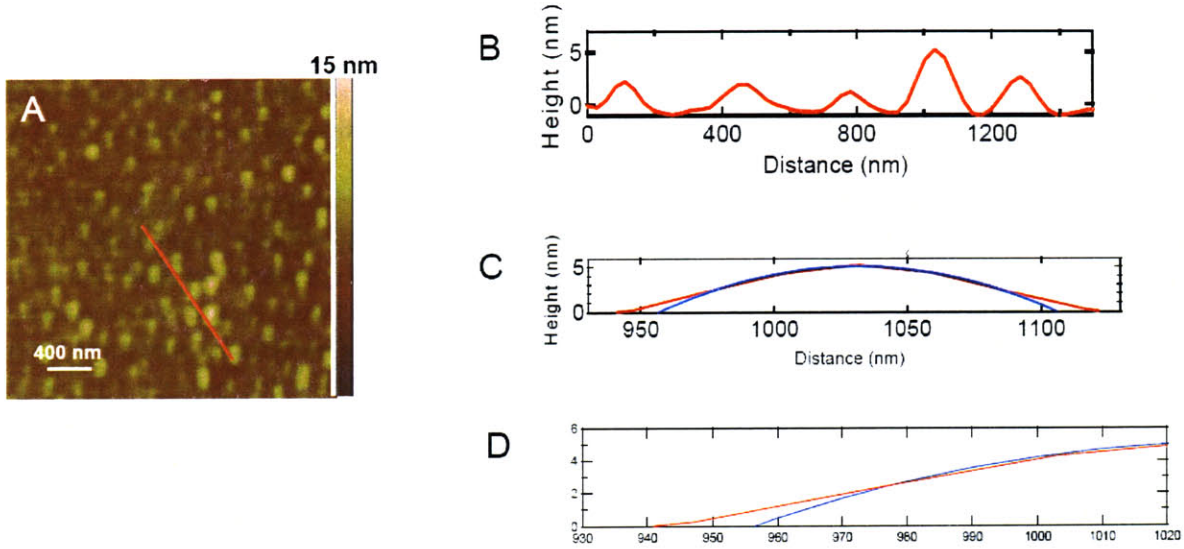

Figure 6.1: Shape analysis of nanobubbles: (A) Tapping-mode AFM height image of PS in water, (B) cross-sectional view along the line drawn in Figure 6.1A, (C) Spherical fit (blue curve) to the actual bubble profile (red curve) corresponding to the bubble, which is enclosed in the box in Fig. 6.1B. (D) The bubble profile along with the spherical cap profile in Fig. 1C as seen close to the three-phase contact line

6.5 Thermodynamic picture

Figure 6.2 shows the schematic diagram showing thermodynamic energy changes near the solid-liquid-vapor interface for the case of nanobubbles sitting on a hydrophobic surface in water. I don't attempt to present any calculations or draw any conclusions based on this diagram. This problem is a potential future work.

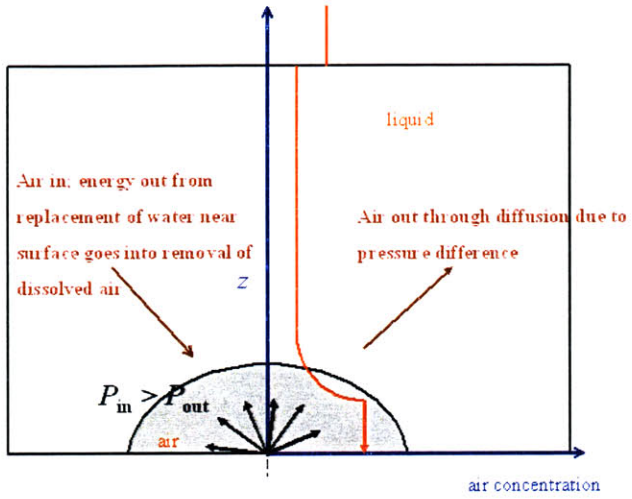

Figure 6.2: Schematic showing thermodynamics processes near solid-liquid-vapor interface for the case of nanobubbles

Chapter 7

Conclusions

7.1 Evaluation of thesis objectives and contributions

We have demonstrated that nanobubbles form spontaneously on flat hydrophobic (silanized silicon oxide and glass wafers, polystyrene) surfaces but not on flat hydrophilic (untreated silicon oxide wafers, PMMA, HOPG) surfaces. However, nanobubbles do appear on hydrophilic silicon surfaces and HOPG upon in-situ mixing of ethanol and water. The formation of nanobubbles in this case is driven by gas separation due to the different solubility of air in the two liquids. Strong experimental evidence has been shown to support the conclusions that nanobubbles can form spontaneously at the interface of polar liquids and hydrophobic surfaces.

Nanobubbles did not form on patterned PMMA surfaces. However, they also did not form on patterned PS surfaces in which the lateral area of PS available for bubble formation was too small to allow nucleation. By increasing the surface area of nanopatterned PS features to several hundred nanometers, though, spontaneous nanobubble formation was observed to occur on the PS domains but not on the surrounding hydrophilic background surface. Thus, by using heterogeneous surfaces with controlled chemistry and lateral size, the location and number density of nanobubbles can be systematically controlled.

While for most part, the shapes of the nanobubbles are well approximated by spherical caps with width much larger than the height; in the vicinity of the three phase contact line, the shapes deviate from the spherical cap profile to merge with the solid surface at a slope of ¡ 0.05. This deviation in the interfacial profile from the spherical cap shape could be due to long-range van der Waals forces, which are relevant at a spatial scale of few nanometers from the solid surface. Nanobubbles are found to be larger in size and less frequent in number with an increase in the hydrophobicity of the solid surface. No effect of line tension forces were observed on the shape of nanobubbles.

From an analytical model available in the literature, we estimate that the present nanobubble morphology may give rise to fluid slip in pressure driven flows with a slip length of 1–2 μm for water flowing over the hydrophobic surface. The consistency of the calculated

slip length with experimental values reported in the literature, suggests that the apparent fluid slip observed experimentally at hydrophobic surfaces may arise from the presence of nanobubbles. The reduction in viscous skin-friction for microscopic flow past surfaces with well-known nanobubble morphology is presently being studied to investigate the influence of the size and number of nanobubbles on frictional stresses.

7.2 Future work

Though there has been a significant advancement in the understanding of nanobubble phenomena, there still are some remaining issues with the stability of nanobubbles which need to be addressed. Following are few ideas which could lead to further research on this subject.

- A full theoretical understanding of the stability of nanobubbles is needed. Effect of long-range forces could play a role in stabilizing the bubbles. This possibility needs to be checked by writing down governing equations starting from fundamental relations.
- Molecular dynamics simulation could also provide interesting insights into formation and existence of nanobubbles. The number of molecules inside a typical nanobubble is ~20,000 (chapter 6), which is a reasonable number to be numerically simulated.
- A few macroscale experiments could be done to measure the reduction in macroscopic friction of fluid flow past the surface with nanobubbles present at the liquid-solid interface. Triborheometry [31] and laser feedback interferometer [30] are few examples of the instruments and techniques, which can be used to measure the frictional properties on surfaces with controlled presence of nanobubbles.
- Topologically smooth but chemically heterogenous surfaces could be studied to study the sole effects of chemical inhomogeneity on nanobubbles in absence of any topographical change.
- It's still not known deterministically as to how hydrophobic a sample needs to be to support nanobubbles. A careful set of experiments with numerous surfaces with different degrees of hydrophobicity can help provide the answer.

Appendix A

Useful tricks for imaging and confirmation of nanobubbles

In this appendix, I detail some of the AFM protocols and image analysis algorithms that were developed for successful imaging of nanobubbles.

- Changing different scan-parameters, e.g. scan-angle, scan-size, and setpoint-voltage while scanning to look for corresponding changes in the images is helpful in knowing whether the features being imaged are real features or artifacts. Quite often, periodic artifacts due to noise, would appear in some of the scans, which if confused as surface patterns would result in spurious conclusions.

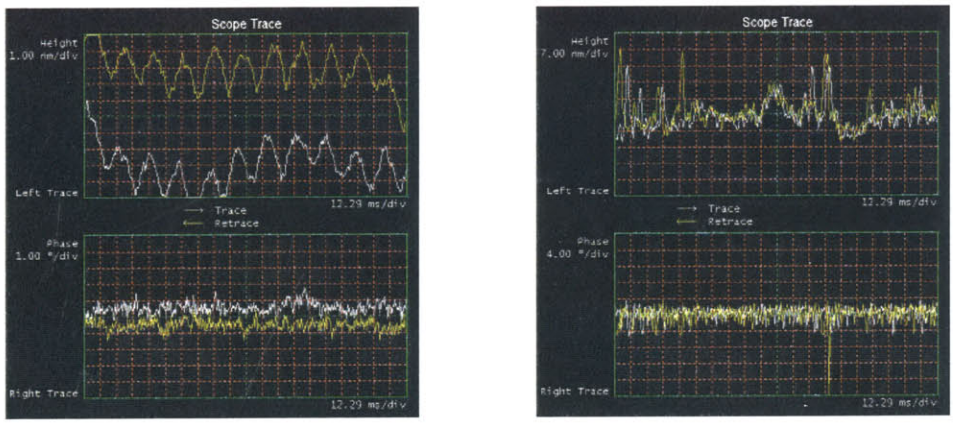

(a) Image corresponding to noise

(b) Image corresponding to real features

Figure A.1: 'Scope mode' images corresponding to noise and real features

- Sometimes, checking the height and phase profiles in 'scope mode' during scanning could be helpful in distinguishing between noise and actual features. Whereas a gradually changing, smooth and overlapping trace and retrace profiles are usually indicative of actual features, profiles with enormously large variations or periodic, sinusoidal variations indicate noise. This observation is shown in Figure A.1.

Silane	sample 1	sample 2	sample 3	sample 4
CTMS	63°	78°	72°	79°
OTS	110°	108°	112°	109°

Table A.1: Contact angle variation on different samples of silane-hydrophobized glass

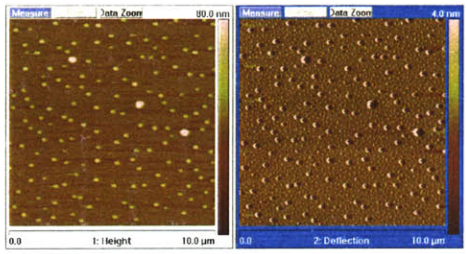

Figure A.2: In-air contact-mode AFM height and deflection images of OTS hydrophobized silicon sample, showing regularly arranged features (contaminants), which could very well be confused with bubbles.

- For the sake of consistency, it is better to carry out all the relevant measurements, viz. contact angle, in-air and in-water AFM imaging, on the same sample. Making observations on the same sample is important as we find in this study that the surface-topology (roughness) and consequently the contact angle value vary within 5–10 degrees from sample to sample. Table A.1 shows the variation in contact angle for same kind of surface on different samples.

- Obtaining a featureless in-air image of a plain hydrophobic sample is necessary before carrying out in-water tapping-mode imaging on the sample. This exercise would take care of the possibility of confusing contaminants (which more often than not are present on the sample surfaces) with nanobubbles. Figure A.2 shows an in-air AFM image of OTS hydrophobized silicon sample. We can see bubble-like features present on the sample, which could only be contaminants in this case, given the sample is imaged in air. If the surfaces had not been imaged in air before they were imaged in water, these features could have been interpreted as bubbles. A rigorous cleaning procedure as discussed in detail in chapter 2 could be used to avoid the presence of contaminants on the surface.

- In this study, bubbles were found to show large variation in morphology upon changing the magnitude of tapping force (Figure 3.7). Figure A.3 shows an image where tapping force was increased in the middle region of the scan area for a short while. This exercise can be carried out to confirm the features as *soft* nanobubbles.

- Use of *fiducial* marks on samples were found to be helpful for scanning of a desired location on the sample. For the AFM instrument in our lab, it was found that if a

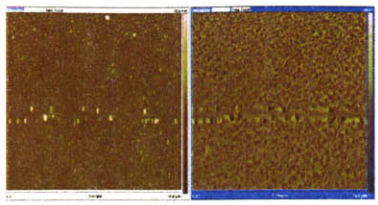

Figure A.3: Change in bubble morphology with change in tapping-force in the middle region of the scan area

sample of size 1.2 cm × 1.2 cm—large enough to prevent liquid oozing out of the fluid cell and small enough to fit into the head—is placed symmetrically on the piezo-tube, AFM probe comes on the top of region close to the center of the sample.

- In few of the experiments in this study as well as in studies in literature [47, 61], piezo-drift is found to be present, giving rise to elliptic-shaped, large-sized, widely-spaced bubbles (Figure A.4). In these cases, one should not take into account these bubbles for quantitative analysis and calculation of bubble parameters.

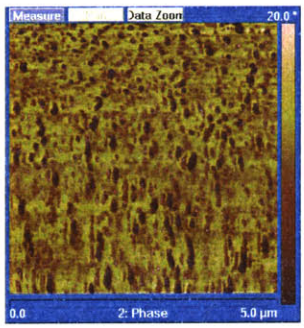

(a) Elliptic-shaped bubbles near the end of scan direction

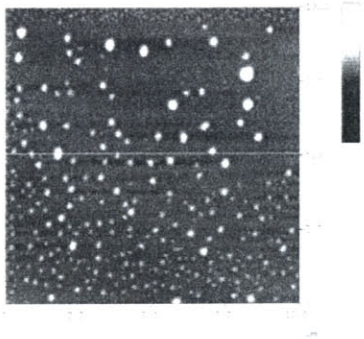

(b) Sparsely located bubbles at the top [61]

Figure A.4: Elliptic-shaped, large-sized, and widely-spaced bubbles near the end of scan direction, occurring due to piezo drift

Appendix B

A summary of results from studies on nanobubbles available in literature

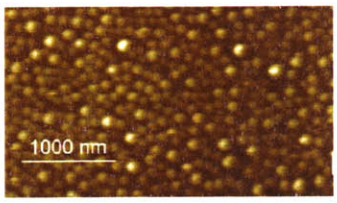

(a) Simonsen *et* al. [47, 51]

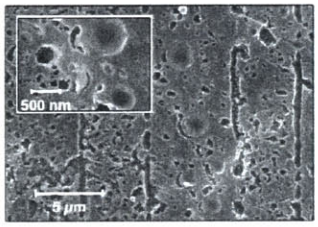

(b) Switkes *et* al. [53]

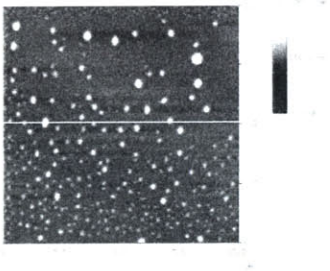

(c) Yang *et* al. [61]

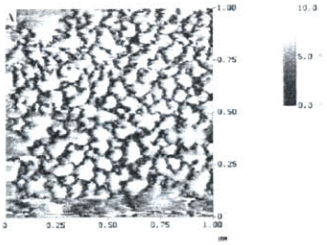

(d) Attard *et* al. [7, 57, 58]

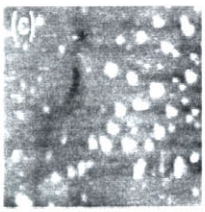

(e) Holmberg *et* al. [24] (scan size: $2\mu m \times 2\mu m$)

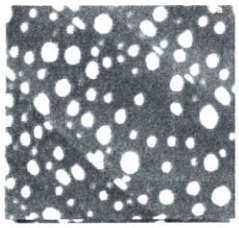

(f) Zhang *et* al. [35, 36, 37, 63, 64] (scan size: $10\mu m \times 10\mu m$)

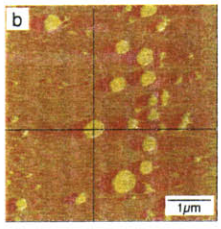

(g) Ishida *et* al. [27, 28]

Figure B.1: Images of nanobubbles obtained by different research groups

Research group	Simonsen *et* al. [47, 51]	Zhang *et* al. [35, 36, 37, 63, 64]	Switkes *et* al. [53]	Yang *et* al. [61]
Surface(s) studied	polystyrene	HOPG, mica	HMDS hydrophobized silicon	TMCS hydrphobized (in-vapor and in-solution) silicon
Imaging technique	magnetic-mode AFM	tapping-mode AFM	*quick-freeze deep etch* (QFDE)	tapping-mode AFM
Contact angle with water, θ (°)	~92	not-mentioned	92	74 (in vapor) 88 (in solution)
Height of nanobubbles (nm)	6.6	not-mentioned	N/A	20–80 (vapor) 60–200 (solution)
Diameter of nanobubbles (nm)	130	not-mentioned	50–500	100–800 (vapor) 300–800 (solution)
Sign of phase-shift across nanobubbles	positive	negative	N/A	positive

Research group	Ishida *et* al. [27, 28]	Attard *et* al. [7, 57, 58]	Holmberg *et* al. [24]
Surface(s) studied	OTS hydrophobized silicon	DMDCS hydrophobized glass	gold
Imaging technique	tapping-mode AFM	tapping-mode AFM	contact- and tapping-mode AFM
Contact angle with water, θ (°)	110	101	100
Height of nanobubbles (nm)	≤40	20–30	0.4–5 (contact mode) ~6 (tapping mode)
Diameter of nanobubbles (nm)	≤650	70–87	50–150
Sign of phase shift across nanobubbles	positive	positive	N/A

Table B.1: Summary of important results from studies on nanobubble available in literature

Appendix C

Sign of phase-change across nanobubbles in tapping-mode AFM

As mentioned in chapter 2, phase imaging is an important tool in the context of this study as it can be useful in confirmation of features observed in the AFM images as nanobubbles or contaminants. A large change in phase angle is observed almost invariably at the location of the nanobubbles, which suggests a distinct difference in material properties at these locations compared to other locations. However, it is still unclear whether the phase should drop or rise across the *soft* nanobubbles.

From Table B.1 given in appendix B, we see that while few studies [27, 58, 61] report an increase in phase-angle at the location of nanobubbles, there are few studies [63, 64], which report a negative change in phase angle across nanobubbles. Since rest of the experimental conditions, including the type of the probe and the medium of operation, are same for all of the above investigations, opposite shifts in phase seems contradictory.

For most of the results in this study, a large negative change in phase is observed at the site of nanobubbles. A larger phase-shift at the locations of nanobubbles are observed as compared to phase shift corresponding to contaminants at other locations. This observation is consistent with the soft nature of nanobubbles [38]. A softer material leads to a larger contact area, which consequently leads to an increase in the duration of tip-sample contact, resulting in a greater phase shift, as compared to a harder material.

However, literature does not seem to agree upon the importance of different factors, which affect the sign of phase-shift. According to Magonov *et* al. [38], shift in phase-angle between the free and interactive cantilevers is given by equation C.1a,

$$\Delta\phi = \frac{Q\sigma}{k} \tag{C.1a}$$

$$\sigma = \sum_i \frac{\partial F_i}{\partial z} \tag{C.1b}$$

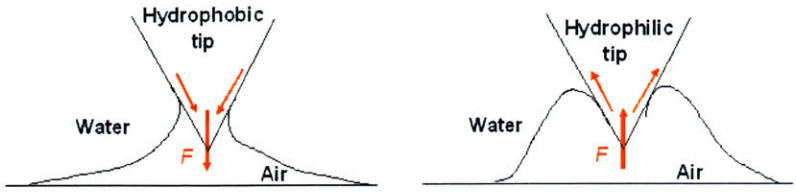

Figure C.1: Force of interaction between nanobubble and hydrophilic and hydrophobic tips

where $\Delta\phi$ is the phase change, Q is the quality factor, k is the spring constant, and σ is sum of force derivative given by equation C.1b. This equation suggests that the sign of phase angle shift coincides with that of the overall force derivative, and thus the phase shift is positive when the overall force acting on the tip is repulsive and negative when the overall force is attractive.

Figure C.1 shows the direction of force of interaction between a nanobubble and hydrophilic and hydrophobic probes. The probe used in this study is made of hydrophilic silicon nitride, which would lead to a repulsive force on the tip according to the above figure. A repulsive force of interaction and a negative change in phase at the location of nanobubbles does not seem to be in agreement with the theory given by Magonov *et* al. [38].

However, in another study, Tamayo *et* al. [54] show that phase contrast can also be a function of energy dissipation in the sample, because of which the dependence of phase angle on surface properties can be more complex.

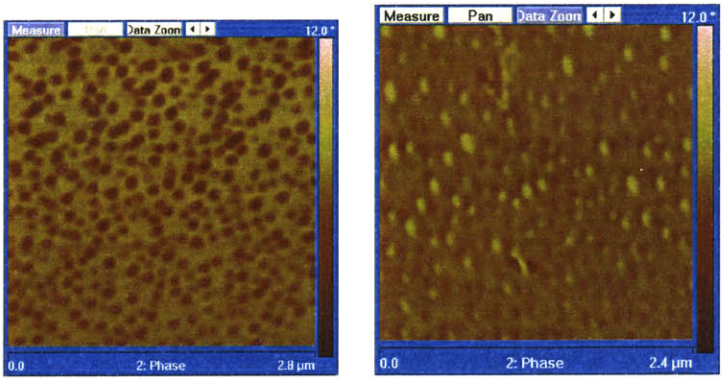

(a) Negative change in phase (b) Positive phase change

Figure C.2: Both positive as well as negative phase changes are observed for nanobubbles imaged in this study (PS is used as the solid substrate here)

From the experiments in this study, it is also found that the phase contrast depends on the magnitude of tapping force (in other words, setpoint voltage) as well. Figure C.2 shows the phase images of nanobubbles on polystyrene surface. Positive phase change as well as negative phase change was observed for nanobubbles with different tapping force.

In conclusion to the above discussion, it can be said that a sharp and large change in phase-angle is a definite indication of the material being softer at that location compared to rest of the region. However, to make any interpretations from the sign of phase shift is difficult and can be ambiguous.

Bibliography

[1] *http://www.ntmdt.com.*

[2] A. Agrawal, J. Park, D. Y. Ryu, P. T. Hammond, T. P. Russell and G. H. McKinley Controlling the location and spatial extent of nanobubbles using hydrophobically nanopatterned surfaces. *Nano Letters*, ASAP.

[3] A. Agrawal and G. H. McKinley An experimental investigation of presence and properties of nanobubbles observed at the solid-liquid interface. *Journal of Colloid and Interface Science*, in preparation.

[4] A. Amirfazli and A. W. Neumann. Status of the three-phase line tension. *Advances in Colloid and Interface Science*, 110(3):121–141, 2004.

[5] P. Attard. Bridging bubbles between hydrophobic surfaces. *Langmuir*, 12(6):1693–1695, 1996.

[6] P. Attard. Patterns of hydrogen bonding in water and ice. *Physica A*, 233(3-4):742–753, 1996.

[7] P. Attard. Friction, adhesion, and deformation: dynamic measurements with the atomic force microscope. *Journal of Adhesion Science and Technology*, 16(7):753–791, 2002.

[8] P. Attard. Nanobubbles and the hydrophobic attraction. *Advances in Colloid and Interface Science*, 104:75–91, 2003.

[9] P. Attard, M. P. Moody, and J. W. G. Tyrrell. Nanobubbles: the big picture. *Physica A-Statistical Mechanics and Its Applications*, 314(1-4):696–705, 2002.

[10] M. Behl, J. Seekamp, S. Zankovych, C. M. S. Torres, R. Zentel, and J. Ahopelto. Towards plastic electronics: Patterning semiconducting polymers by nanoimprint lithography. *Advanced Materials*, 14(8):588–591, 2002.

[11] J. Bico, C. Marzolin, and D. Quere. Pearl drops. *Europhysics Letters*, 47(6):743–744, 1999.

[12] G. Binning, H. Rohrer, C. Gerber, and E. Weibel. Surface studies by scanning tunneling microscopy. *Physical Review Letters*, 49(1):57–61, 1982.

[13] R. Blossey. Self-cleaning surfaces - virtual realities. *Nature Materials*, 2(5):301–306, 2003.

[14] A. Carambassis, L. C. Jonker, P. Attard, and M. W. Rutland. Forces measured between hydrophobic surfaces due to a submicroscopic bridging bubble. *Physical Review Letters*, 80(24):5357–5360, 1998.

[15] A. B. D. Cassie and S. Baxter. Wettability of porous surfaces. *Transaction of Faraday Society*, 40:546, 1944.

[16] A. W. Chow. Lab-on-a-chip: Opportunities for chemical engineering. *Aiche Journal*, 48(8):1590–1595, 2002.

[17] H. K. Christenson and P. M. Claesson. Direct measurements of the force between hydrophobic surfaces in water. *Advances in Colloid and Interface Science*, 91(3):391–436, 2001.

[18] C. Cottin-Bizonne, J. L. Barrat, L. Bocquet, and E. Charlaix. Low-friction flows of liquid at nanopatterned interfaces. *Nature Materials*, 2(4):237–240, 2003.

[19] V. S. J. Craig, B. W. Ninham, and R. M. Pashley. Direct measurement of hydrophobic forces: A study of dissolved gas, approach rate, and neutron irradiation. *Langmuir*, 15(4):1562–1569, 1999.

[20] D. R. Evans, V. S. J. Craig, and T. J. Senden. The hydrophobic force: nanobubbles or polymeric contaminant? *Physica a-Statistical Mechanics and Its Applications*, 339(1-2):101–105, 2004.

[21] P. G. de Gennes. Wetting: statics and dynamics *Review of Modern Physics*, 57:827–863, 1985.

[22] S. Granick, Y. X. Zhu, and H. Lee. Slippery questions about complex fluids flowing past solids. *Nature Materials*, 2(4):221–227, 2003.

[23] S. Herminghaus. Roughness-induced non-wetting. *Europhysics Letters*, 52(2):165–170, 2000.

[24] M. Holmberg, A. Kuhle, J. Garnaes, K. A. Morch, and A. Boisen. Nanobubble trouble on gold surfaces. *Langmuir*, 19(25):10510–10513, 2003.

[25] Micronics Inc. *http://www.micronics.net/.*

[26] Digital Instruments. *Multimode SPM Instruction Manual.*

[27] N. Ishida, T. Inoue, M. Miyahara, and K. Higashitani. Nano bubbles on a hydrophobic surface in water observed by tapping-mode atomic force microscopy. *Langmuir*, 16(16):6377–6380, 2000.

[28] N. Ishida, M. Sakamoto, M. Miyahara, and K. Higashitani. Optical observation of gas bridging between hydrophobic surfaces in water. *Journal of Colloid and Interface Science*, 253(1):112–116, 2002.

[29] J. Israelachvili and R. Pashley. The hydrophobic interaction is long-range, decaying exponentially with distance. *Nature*, 300(5890):341–342, 1982.

[30] H. P. Kavehpour, B. Orvyn and G. H. McKinley. The microscopic and macroscopic structure of the precursor layer in spreading viscous drops. *Physical Review Letters*, 91(19):art. no.–196104, 2003.

[31] H. P. Kavehpour and G. H. McKinley. Tribo-rheometry: from gap-dependent rheology to tribology. *Tribology Letters*, 17:327–335, 2004.

[32] Y. S. Kim, S. J. Baek, and P. T. Hammond. Physical and chemical nanostructure transfer in polymer spin-transfer printing. *Advanced Materials*, 16(7):581–584, 2004.

[33] s A. Lafuma and D. Quere. Superhydrophobic states. *Nature Materials*, 2(7):457–460, 2003.

[34] E. Lauga and M. P. Brenner. Dynamic mechanisms for apparent slip on hydrophobic surfaces. *Physical Review E*, 70(2), 2004. Part 2.

[35] S. T. Lou, J. X. Gao, X. D. Xiao, X. J. Li, G. L. Li, Y. Zhang, M. Q. Li, J. L. Sun, and J. Hu. Nanobubbles at the liquid/solid interface studied by atomic force microscopy. *Chinese Physics*, 10:S108–S110, 2001. Suppl. S.

[36] S. T. Lou, J. X. Gao, X. D. Xiao, X. J. Li, G. L. Li, Y. Zhang, M. Q. Li, J. L. Sun, X. H. Li, and J. Hu. Studies of nanobubbles produced at liquid/solid interfaces. *Materials Characterization*, 48(2-3):211–214, 2002.

[37] S. T. Lou, Z. Q. Ouyang, Y. Zhang, X. J. Li, J. Hu, M. Q. Li, and F. J. Yang. Nanobubbles on solid surface imaged by atomic force microscopy. *Journal of Vacuum Science and Technology B*, 18(5):2573–2575, 2000.

[38] S. N. Magonov, V. Elings, and M. H. Whangbo. Phase imaging and stiffness in tapping-mode atomic force microscopy. *Surface Science*, 375(2-3):L385–L391, 1997.

[39] J. Mahnke, J. Stearnes, R. A. Hayes, D. Fornasiero, and J. Ralston. The influence of dissolved gas on the interactions between surfaces of different hydrophobicity in aqueous media part i. measurement of interaction forces. *Physical Chemistry Chemical Physics*, 1(11):2793–2798, 1999.

[40] M. Mao, J. H. Zhang, R. H. Yoon, and W. A. Ducker. Is there a thin film of air at the interface between water and smooth hydrophobic solids? *Langmuir*, 20(5):1843–1849, 2004.

[41] E. E. Meyer, Q. Lin, and J. N. Israelachvili. Effects of dissolved gas on the hydrophobic attraction between surfactant-coated surfaces. *Langmuir*, 21(1):256–259, 2005.

[42] J. L. Parker, P. M. Claesson, and P. Attard. Bubbles, cavities, and the long-ranged attraction between hydrophobic surfaces. *Journal of Physical Chemistry*, 98(34):8468–8480, 1994.

[43] R. M. Pashley, P. M. McGuiggan, B. W. Ninham, and D. F. Evans. Attractive forces between uncharged hydrophobic surfaces - direct measurements in aqueous-solution. *Science*, 229(4718):1088–1089, 1985.

[44] D. Quere. Rough ideas on wetting. *Physica A-Statistical Mechanics and Its Applications*, 313(1-2):32–46, 2002.

[45] T. P. Russell, T. Thurn-Albrecht, Z. Q. Lin, T. Kerle, T. Xu, M. Tuominen, E. Schaeffer, and U. Steiner. Patterning polymers from the nanoscopic to microscopic size scales. *Abstracts of Papers of the American Chemical Society*, 221:U384–U385, 2001. Part 2.

[46] T. P. Russell, T. Xu, B. M. Ocko, O. Gang, and A. Gibaud. Surface reconstruction: A simple route to reversible nanoporous templates. *Abstracts of Papers of the American Chemical Society*, 227:U516–U516, 2004. Part 2.

[47] A. C. Simonsen, P. L. Hansen, and B. Klosgen. Nanobubbles give evidence of incomplete wetting at a hydrophobic interface. *Journal of Colloid and Interface Science*, 273(1):291–299, 2004.

[48] D. R. E. Snoswell, J. M. Duan, D. Fornasiero, and J. Ralston. Colloid stability and the influence of dissolved gas. *Journal of Physical Chemistry B*, 107(13):2986–2994, 2003.

[49] V. P. Sokhan, D. Nicholson, and N. Quirke. Fluid flow in nanopores: An examination of hydrodynamic boundary conditions. *Journal of Chemical Physics*, 115(8):3878–3887, 2001.

[50] V. P. Sokhan, D. Nicholson, and N. Quirke. Fluid flow in nanopores: Accurate boundary conditions for carbon nanotubes. *Journal of Chemical Physics*, 117(18):8531–8539, 2002.

[51] R. Steitz, T. Gutberlet, T. Hauss, B. Klosgen, R. Krastev, S. Schemmel, A. C. Simonsen, and G. H. Findenegg. Nanobubbles and their precursor layer at the interface of water against a hydrophobic substrate. *Langmuir*, 19(6):2409–2418, 2003.

[52] K. W. Stockelhuber, B. Radoev, A. Wenger, and H. J. Schulze. Rupture of wetting films caused by nanobubbles. *Langmuir*, 20(1):164–168, 2004.

[53] M. Switkes and J. W. Ruberti. Rapid cryofixation/freeze fracture for the study of nanobubbles at solid-liquid interfaces. *Applied Physics Letters*, 84(23):4759–4761, 2004.

[54] J. Tamayo and R. Garcia. Effects of elastic and inelastic interactions on phase contrast images in tapping-mode scanning force microscopy. *Applied Physics Letters*, 71(16):2394–2396, 1997.

[55] A. Terray, J. Oakey, and D. W. M. Marr. Microfluidic control using colloidal devices. *Science*, 296(5574):1841–1844, 2002.

[56] D. C. Tretheway, C. D. Meinhart. A generating mechanism for apparent fluid slip in hydrophobic microchannels. *Physics of FLuids*, 16:1509–1515, 2004.

[57] J. W. G. Tyrrell and P. Attard. Images of nanobubbles on hydrophobic surfaces and their interactions. *Physical Review Letters*, 8717(17):art. no.–176104, 2001.

[58] J. W. G. Tyrrell and P. Attard. Atomic force microscope images of nanobubbles on a hydrophobic surface and corresponding force-separation data. *Langmuir*, 18(1):160–167, 2002.

[59] R. N. Wenzel. Surface roughness and contact angle. *Industrial Engineering Chemistry*, 28:988–994, 1936.

[60] G. M. Whitesides and A. D. Stroock. Flexible methods for microfluidics. *Physics Today*, 54(6):42–48, 2001.

[61] J. W. Yang, J. M. Duan, D. Fornasiero, and J. Ralston. Very small bubble formation at the solid-water interface. *Journal of Physical Chemistry B*, 107(25):6139–6147, 2003.

[62] Q. L. Zhang, T. Xu, T. P. Russell, and T. Emrick. Hybrid materials composed of colloidal nanoparticles and polymers: Directed deposition and self-assembly. *Abstracts of Papers of the American Chemical Society*, 228:U466–U466, 2004. Part 1.

[63] X. H. Zhang and H. Jun. Nanobubbles at the solid/water interface. *Progress in Chemistry*, 16(5):673–681, 2004.

[64] X. H. Zhang, X. D. Zhang, S. T. Lou, Z. X. Zhang, J. L. Sun, and J. Hu. Degassing and temperature effects on the formation of nanobubbles at the mica/water interface. *Langmuir*, 20(9):3813–3815, 2004.

[65] Y. X. Zhu and S. Granick. Rate-dependent slip of newtonian liquid at smooth surfaces. *Physical Review Letters*, 8709(9):art. no.–096105, 2001.